Fluid flow and sperm guidance: a simulation study of hydrodynamic sperm rheotaxis.

AUTHOR(S):

Ishimoto, Kenta; Gaffney, Eamonn A

Fluid flow and sperm guidance: a simulation study of hydrodynamic sperm rheotaxis

Kenta Ishimoto[1,2*] and Eamonn A. Gaffney[3†]

[1] The Hakubi Center for Advanced Research, Kyoto University, Kyoto, 606-8501, Japan
[2] Research Institute for Mathematical Sciences, Kyoto University, Kyoto, 606-8502, Japan
[3] Wolfson Centre for Mathematical Biology, Mathematical Institute, University of Oxford, Oxford OX2 6GG, UK

Abstract

How does a sperm find its way? The study of guidance cues has fascinated sperm biologists and in particular the prospect of rheotaxis, that is a fluid flow orienting the direction of sperm swimming, has been the subject of extensive recent study, as readily motivated by the prospect that such guidance may be active in the mammalian female reproductive tract. For instance, it has been hypothesised that helical sperm flagellar beating is necessary for such guidance, whereas there is an extensive diversity of flagellar beating patterns, with planar sperm beating readily observed in human cells for example. In particular, such cells will not be guided by fluid flow according to hypothesised mechanisms for rheotaxis presented thus far. Here, using simulation methods, we investigate rheotaxis for a wide range of flagellar beat patterns. Providing the virtual sperm firstly does not possess a tightly circling trajectory in the absence of a background flow and secondly remains within a region of low shear to prevent being washed away by the background flow, rheotaxis is generally observed with the sperm swimming into the flow together with a possible transverse velocity. Tight circling sperm motility, as observed in select hyperactivated sperm and CatSper mutants, is predicted to disrupt the rheotactic response, whilst confinement to low shear regions generally requires boundary accumulation, thus introducing subtleties in the relationship between rheotactic behaviours and the flagellar waveform and sperm characteristics. Nonetheless such predictions suggest such rheotactic guidance may be more common and robust than previously thought and we document simple criteria for the presence of rheotaxis that are consistent with our simulations and understanding, as well as reported observations to date.

Keywords: sperm motility, low Reynolds number flow, sperm guidance, shear flow

*ishimoto@kurims.kyoto-u.ac.jp
†gaffney@maths.ox.ac.uk

1 Introduction

A fundamental question concerning spermatozoan dynamics is guidance: how does a sperm know where to go, or indeed, does it, or is it merely a case that so many sperm are released that random motility is nonetheless sufficient. However, following insemination in humans, the observed presence at any given time of only 10-1000 sperm within the expanse of the fallopian tubes suggest randomness alone is implausible in bringing the sperm to the egg at this point [7], whilst highly directed motility is also recorded in video-microscopy of sperm motility in the bovine female reproductive tract [18]. Furthermore, marine external fertilisers such as sea urchin sperm exhibit an extensive chemotactic response [31], which is reported to improve the chances of reproductive success [35] and is reviewed by Alvarez et al. [1].

Such observations of sea urchin sperm have previously generated the hypothesis that chemotaxis is also important for mammals [22] and a further suggested mammalian sperm guidance mechanism is thermotaxis [2], which is based on very small temperature differences along the mammalian reproductive tract. More generally, there are extensive reports of chemotactic and thermotactic responses (e.g. [2, 22]), as reviewed in a recent monograph [5], highlighting the possibility that these mechanisms may be active in mammalian reproduction. However, in contrast, the specific role of chemotaxis and thermotaxis is reported as not established for mammals and there are conflicting reports of mammalian spermatozoan response to thermal gradients [21]. Furthermore, both mammalian chemotaxis and thermotaxis require the maintenance of a detectable, robust, signal throughout substantial regions of the female reproductive tract for long range guidance. Thus, the prospective disruption of gradients due to peristalsis and ciliary flows has led to the consequent suggestion that long range biochemical cues are not stable in-situ [16], with analogous reasoning immediately relevant for thermotactic gradients.

In addition to the above explorations of prospective chemotactic and thermotactic guidance for mammalian sperm, the presence of directed flows in the female reproductive tract, such as the ciliary flows in the video-microscopy of Kölle et al. [18], has also generated the hypothesis that rheotaxis, i.e. the bias of sperm swimming by the direction of fluid flow, may provide a guidance cue [21]. Rheotaxis, with sperm directed to swim into the current, was first reported over a century ago [19] and many times in past decades [4, 25, 32], though more recent studies have documented the rheotactic response for a variety of sperm in further detail, as well as emphasising its prospective importance in the female mammalian reproductive tract. For instance, it has been observed that sea urchin sperm are not biased by fluid flow, nor are CatSper mutant sperm, which possess defective calcium signal transduction, whilst normal motile uncapacitated mouse sperm undergo rheotaxis, as do headless sperm [21]. Further independent observations of uncapacitated normal human and bull sperm rheotaxis [16] are also reported, in studies which additionally emphasise that velocity components transverse to the flow profiles can occur.

Summarising their observations led Miki and Clapham [21] to the hypothesis that sperm rheotaxis requires shear flow, boundary accumulation and a three dimensional helicoid beat pattern, that is also associated with sperm rolling [21]. Kantsler et al. [16] also distinguished helicoid flagellar waveforms for the observed boundary accumulation in their study and constructed a minimal model for the boundary accumulating rheotactic response. This formulation was based on the reorientation of a tilted conical helix, representing the flagellum in shear flow, via an asymptotic limit of a resistive force theory calculation. In addition, the sperm head was hardwired to remain near the boundary and to swim in a straight line on average and the no-slip conditions were not enforced on the boundary.

Parameter	Interpretation	Value
L	Flagellar length	56μm
$1/T = \omega/[2\pi]$	Beat frequency	14 Hz
α	Chirality parameter	$\pm\{0, 0.01, 0.05, 0.1, 0.2\}$
Γ/L	Asymmetric waveform parameter	$\{0.5, \infty\}$
kL	Wavenumber	3π
B	Flagellar envelope parameter	$0.2L$
a	Flagellar radius	$0.01L$

Table 1: Reference parameter values for the flagellum waveform, with details on the motivation for the parameter estimates presented in section 1 of the *Supplementary Information*.

Under such conditions the model will always predict rheotaxis, as the tilted conical helix always aligns its major axis with flow and analogous deductions of rheotaxis in the framework would hold for the planar rigid filament formed by projecting the conical helix onto a plane containing the cone's axis of symmetry (set the chirality parameter $\chi = 0$ in equation (41) within Kantsler et al.'s supplementary information).

However boundary accumulation is hardwired in such modelling predictions yet, physically, this is a subtle effect [9, 28, 15] with detailed features, such as sensitivity to flagellar wavenumber or the onset of hyperactivation, that are difficult to reconcile within simplified theories [27] and beyond the intended scope of Kantsler et al.'s modelling framework [16]. More generally, it is not physically clear when and if boundary accumulation can be disrupted by background flow especially for changes in the flagellar beat pattern, and thus the extent to which sperm guidance based on rheotaxis in the vicinity of a surface is contingent on the flagellar waveform. Furthermore, the characteristics of the boundary accumulating, rheotactic sperm considered in both Miki and Clapham [21] and Kantsler et al. [16] correspond to one suggested modality of boundary accumulation with elliptic helicoid flagellar beating [34, 28], whereas a further modality of boundary accumulation, with planar beating and straight swimming is also regularly observed in more viscous media both for human [29] and rat [34]. According to Miki and Clapham's hypotheses [21], sperm under these circumstances will not rheotax, with the prospective implication that the rheotactic response may differ substantially among species and/or according to detailed conditions. However, a physical representation of sperm swimming with the ingredients required to assess the presence or absence of boundary accumulating rheotaxis has not yet been explored, even in modelling studies.

Consequently, our first objective is to use hydrodynamic numerical simulation in an investigation of boundary accumulating sperm rheotaxis, resolving the geometrical complexity of the flagellar wave form and the impact of the surface. This will allow the consideration of numerous questions, such as testing whether the mechanism presented by Miki and Clapham [21] generates rheotaxis and whether such dynamics requires an elliptical helicoid beat or whether planar flagellar waveforms can also feasibly induce rheotaxis. This additional modelling resolution will also enable the further objectives of considering if the absence of rheotaxis in sea urchin sperm and mammalian CatSper mutants can be explained in the context of physics, rather than a detailed systems biological response, as well as briefly considering the impact of hyperactivation on the prospects of sperm rheotaxis.

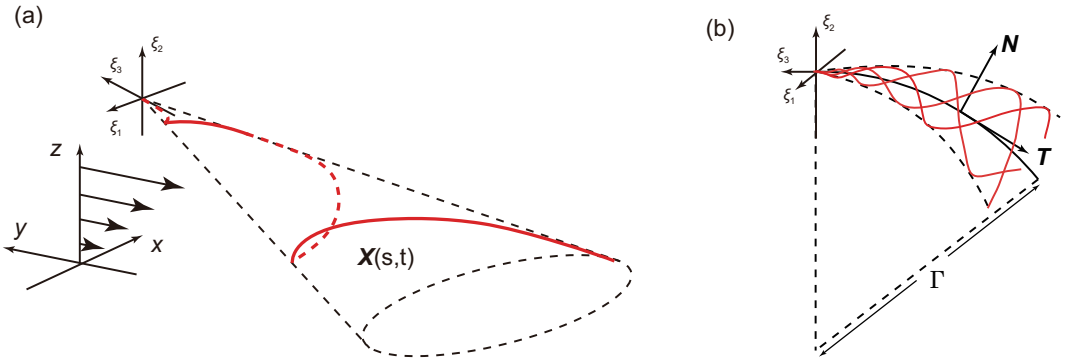

Figure 1: Reference frames and flagellar waveforms. A schematic picture illustrating the flagellar waveforms together with the reference frames. (a) The flagellar reference frame, which is right-handed, and a typical symmetric elliptical helicoid flagellar profile, as depicted in red, with $\boldsymbol{X}(s,t)$ denoting the position in the laboratory reference frame for the location at time t and arclength s along the flagellum from the origin of the flagellar reference frame, $\boldsymbol{\xi} = \boldsymbol{0}$. The background shear flow is also depicted relative to the laboratory reference frame, $\boldsymbol{x}$. (b) The asymmetric flagellar waveform. The centreline of a curvilinear elliptical cone is the arc of a circle of radius Γ, with unit tangent $\boldsymbol{T}$, unit normal $\boldsymbol{N}$ and, not depicted, unit binormal $\boldsymbol{B} = \boldsymbol{T} \wedge \boldsymbol{N}$. The flagellar wave forms a helix on this cone at any snapshot of time, with the flagellum at three different snapshots of time illustrated in red. For both (a) and (b) the time evolution of the flagellum profile corresponds to a wave propagating on the cone, away from the origin of the flagellum reference frame, $\boldsymbol{\xi} = \boldsymbol{0}$.

2 The Virtual Sperm and Its Numerical simulation

Throughout the specification of a virtual sperm and the fluid dynamical equations, we use $\boldsymbol{\xi}$ to denote right-handed Cartesian coordinates fixed in a sperm flagellum reference frame, whose origin is located at the proximal end of the flagellum, with an associated orthonormal basis $\{\boldsymbol{e}_{\xi_i}\}$, $i \in \{1,2,3\}$. In addition we define $\boldsymbol{x} = (x_1, x_2, x_3) := (x, y, z)$ to be Cartesian coordinates fixed in the inertial reference frame of the laboratory, with orthonormal basis $\{\boldsymbol{e}_i\}$, $i \in \{1,2,3\}$.

2.1 The Virtual Sperm Flagellum

Given the importance attached to an elliptical helicoid waveform in recent experimental studies of rheotaxis [21, 16] we focus on this beat pattern, initially with a conical envelope which is symmetric around the ξ_3 axis, as illustrated in Fig. 1(a). The waveform is specified in the flagellar reference frame, $\boldsymbol{\xi}$, with a propagating wave, of wavenumber k and angular frequency ω, parameterised by time, t, and arclength, $s \in [0, L]$ where L is the flagellum length. Thus we have $\boldsymbol{\xi}(s,t) = (\xi_1(\xi_3), \xi_2(\xi_3), \xi_3) = (-\alpha B\mathcal{C}, B\mathcal{C}, \xi_3)$ where α corresponds to the chirality of the wave, with $\alpha = 0$ constituting a planar waveform, $\alpha > 0$ a right handed helix as found in mouse [34] and $\alpha < 0$ gives a left handed helix, as observed for human sperm with $\alpha = -0.2$ [11, 12]. Furthermore, B is a measure of the waveform

amplitude, $\mathcal{C} := \cos(k\xi_3 - \omega t)$ and

$$s(\xi_3) = \int_{\xi_3}^{0} \mathrm{d}\hat{\xi}_3 \left[1 + \left\{\frac{\mathrm{d}\xi_1}{\mathrm{d}\hat{\xi}_3}(\hat{\xi}_3)\right\}^2 + \left\{\frac{\mathrm{d}\xi_2}{\mathrm{d}\hat{\xi}_3}(\hat{\xi}_3)\right\}^2\right]^{1/2}, \tag{2.1}$$

takes values in $[0, L]$, as depicted in Fig 1.

To generate asymmetric waveforms, the axis of symmetry of the enveloping cone of the elliptical helicoid is mapped onto a segment of a circle of radius Γ, given by $(\Gamma - \xi_2)^2 + (\xi_3)^2 = \Gamma^2$, with an orientation given by the direction of decreasing ξ_3, as shown by the centreline in Fig. 1b. Let $\bar{\xi}_3$ denote distance along this curve, with $\bar{\xi}_1$, $\bar{\xi}_2$ normal and binormal coordinates and let $\mathbf{T}, \mathbf{N}, \mathbf{B}$ denote the tangent, normal and binormal unit vectors. Then the asymmetric waveform is given by

$$\begin{aligned} \boldsymbol{\xi}(s,t) &= \bar{\xi}_1(\bar{\xi}_3)\mathbf{N}(\bar{\xi}_3) + \bar{\xi}_2(\bar{\xi}_3)\mathbf{B}(\bar{\xi}_3) + \int_{\bar{\xi}_3}^{0} d\hat{\xi}_3\ \mathbf{T}(\hat{\xi}_3) \\ &= [-\alpha B\mathcal{C}]\,\mathbf{N}(\bar{\xi}_3) + [B\mathcal{C}]\,\mathbf{B}(\bar{\xi}_3) + \int_{\bar{\xi}_3}^{0} d\hat{\xi}_3\ \mathbf{T}(\hat{\xi}_3), \qquad (2.2) \\ s(\bar{\xi}_3) &= \int_{\bar{\xi}_3}^{0} \mathrm{d}\hat{\xi}_3 \left[1 + \left\{\frac{\mathrm{d}\bar{\xi}_1}{\mathrm{d}\hat{\xi}_3}(\hat{\xi}_3)\right\}^2 + \left\{\frac{\mathrm{d}\bar{\xi}_2}{\mathrm{d}\hat{\xi}_3}(\hat{\xi}_3)\right\}^2\right]^{1/2}, \qquad (2.3) \end{aligned}$$

where $\mathcal{C} := \cos(k\bar{\xi}_3 - \omega t)$ and $s \in [0, L]$.

We denote the position of the flagellum at time t and arclength s relative to the laboratory frame by $\boldsymbol{X}(s,t)$, which is given by mapping $\boldsymbol{\xi}(s,t)$ from the flagellum reference frame to the laboratory. Initially, the sperm is located at $\boldsymbol{X}(s=0, t=0) = (0, 0, 0.1L)$ and its orientation is such that $\boldsymbol{e}_{\xi_3}$ is in the x-z plane pointing in the direction of increasing x (see the *Supplementary Information* for a demonstration that the initial orientation in the x-y plane does not alter the final dynamics). Finally, the initial acute angle of attack between $\boldsymbol{e}_1$ and $\boldsymbol{e}_{\xi_3}$, that is $\theta_{init} := \cos^{-1}(\boldsymbol{e}_1 \cdot \boldsymbol{e}_{\xi_3})$, is given by either (i) $\theta_{init} = 0$ or (ii) $\theta_{init} = 0.2\pi$.

2.2 The Virtual Sperm Head: A Modelling Estimate in Justifying its Neglect

For sperm, the head is relatively small compared to the lengthscale of the flagellum and so in Section 2 of the *Supplementary Information* we consider the errors associated with neglecting the head in calculating sperm trajectories, especially their curvature and thus the impact of rheotactic guidance cues. We demonstrate that classical calculations reveal a neglect of the sperm head induces relative errors of about 20% in the swimming speed, whereas the torques due to a sperm head are about three orders of magnitude smaller than those due to the flagellum, and hence head torques are negligible.

Hence neglecting the sperm head entails that angular velocities are generally accurate and linear velocities are of the correct scale; furthermore the predicted linear velocities are *overestimates* as the head increases drag. This entails that the sperm is predicted to swim further for a given change in its orientation and hence its trajectory curvature is underestimated. In this paper the sperm head is neglected and thus rheotactic effects are marginally *underestimated*, though the qualitative details are correct, as confirmed by the observation that headless spermatozoa rheotax in the same manner as cells with standard morphologies [21]. Finally, we note that further modelling uncertainties entail that

Parameter	Interpretation	Value
$\dot{\gamma}$	Background shear flow strength	$0.1T^{-1}$
g/μ	Repulsion potential magnitude	$10LT^{-1}$
d	Repulsion potential lengthscale	$0.005L$

Table 2: Reference parameter values for the shear flow and the surface repulsion potential, noting that μ is the fluid viscosity with details on the motivation for the parameter estimates in Section 1 of the *Supplementary Information*.

the increased computational complexity of including head corrections would be poorly motivated, as detailed further below.

2.3 Determining the Sperm Trajectory and the Possibility of a Rheotactic Response

We have the location of the flagellum relative to the flagellum reference frame, which moves at an *a priori* unknown velocity, $\boldsymbol{U}$, and angular velocity, $\boldsymbol{\Omega}$, relative to the laboratory frame. Taking into account the presence of a no-slip surface, located at $x_3 = 0$ and a half-space domain $x_3 \geq 0$, or other boundary conditions as appropriate, we proceed to overview how low Reynolds number fluid dynamics can determine $\boldsymbol{U}$, $\boldsymbol{\Omega}$. These can then be integrated to construct the sperm trajectory and rheotaxis is predicted if the trajectory associated with the sperm turns into, or away from, the direction of a background flow.

2.3.1 The flow field and the background flow field

Let $p(\boldsymbol{x})$, $\boldsymbol{u}(\boldsymbol{x})$ denote the pressure and velocity field, with $p^{\infty}(\boldsymbol{x})$, $\boldsymbol{u}^{\infty}(\boldsymbol{x})$ the pressure and velocity associated with the background flow, assumed throughout this study to be the solution of Stokes' equation for a linear shear flow

$$p^{\infty}(\boldsymbol{x}) = 0, \qquad \boldsymbol{u}^{\infty}(\boldsymbol{x}) = -\dot{\gamma} x_3 \mathbf{e}_2, \tag{2.4}$$

with $\dot{\gamma} = 0.1T^{-1}$, where T is the sperm flagellum beat period.

2.3.2 The surface potential

We also assume a repulsion potential at very close distances to $z = 0$ to prevent the sperm crashing into this boundary, which is generally a no-slip solid surface in this study, though other boundary conditions are considered, particularly to ascertain the influence of the boundary on sperm dynamics.

Surface repulsion potentials are observed on bringing cells close to a surface, on the scale of tens to one hundred nanometres, but the quantitative details depend on the cell, the surface and the physiological solutes [17]. In effect, we are assuming that the sperm is repelled from the surface at molecular scales, as achieved for human sperm experiments with glassware using dilute human serum albumin [29]. As

motivated in the *Supplementary Information*, a simple repulsive potential is used [30] and the body force per unit length of the flagellum is given by

$$\boldsymbol{f}^{rep} = g\frac{\mathrm{e}^{-x_3/d}}{1-\mathrm{e}^{-x_3/d}}\mathbf{e}_3 = \nabla\psi^{rep}, \qquad \psi^{rep} = gd\ln(1-\mathrm{e}^{-x_3/d}), \tag{2.5}$$

with $g = 10\mu LT^{-1}$ a measure of the overall repulsion, where μ is the fluid viscosity. The parameter $d = 0.005L = 280$nm is a measure of the repulsion potential decay length, which is larger than the scale of 50nm observed for bacteria [17] but details this close to the surface are qualitative only as the surface potential varies with cell, solute and surface and is not documented for sperm.

The impact of variation in d on the quantitative details of trajectory curvatures is briefly presented in Section 3 of the *Supplementary Information* where it can be seen that d influences trajectory curvatures, though not the qualitative details. Thus the surface potential represents a source of modelling uncertainty which mitigates against the additional computational expense of including a sperm head in the modelling.

2.3.3 The prediction of sperm swimming trajectories

By linearity $p - p^{\infty}$, $\boldsymbol{u} - \boldsymbol{u}^{\infty}$ also satisfy Stokes' equations. The solution of these equations yield the instantaneous velocity, $\boldsymbol{U}$, and angular velocity $\boldsymbol{\Omega}$ of the virtual sperm at a fixed time point, given the virtual sperm is subject to the forces from the repulsive surface potential force which prohibits swimming distances closer than approximately $2d$ from the surface at $z = 0$.

This is detailed in Section 3 of the *Supplementary Information,* where the numerical algorithm, the Regularised Stokeslet Method [6, 10], is described and validated in depth. One must note that the solutions differ significantly according to the boundary conditions imposed at $z = 0$, with the imposition of no-slip referred to as the Blakelet solution, since the Regularised Stokeslet Method uses solutions to Stokes equations known as Blakelets [3] in the numerical procedures. For analogous reasons the solutions associated with a fixed tangential stress, matching that of the background shear flow, and no normal velocity at $z = 0$ are referred to as Imagelet solutions [14] and the solutions with no constraints at $z = 0$ are referred to as Stokeslet solutions [24]. Note that the imposition of a fixed tangential stress and zero normal velocity at $z = 0$ corresponding to the Imagelet solutions, may not be relevant in most physical situations, and similarly for the Stokeslet solution given the surface repulsion potential force is retained. Nonetheless, these solutions are extremely informative in assessing the extent to which hydrodynamic interactions between the surface and the cell influence the rheotactic response in interpreting the results below.

Finally, once one can determine the instantaneous velocity, $\boldsymbol{U}$, and angular velocity $\boldsymbol{\Omega}$ of the sperm cell, its position is updated – iterating, the virtual sperm swimming trajectory can be constructed, again as detailed and validated in Section 3 of the *Supplementary Information*.

In turn these numerical predictions will allow the exploration of the propensity for a virtual sperm to rheotax, that is for the sperm to possess a swimming trajectory whose direction is biased by the presence of a background flow. It will also enable a study of how rheotactic behaviour is related to boundary accumulation, i.e. swimming indefinitely in a region of low shear near the interface at $z = 0$, which characterises the origin of the repulsive surface potential used throughout this study and typically, but not always, is modelled as a no-slip surface.

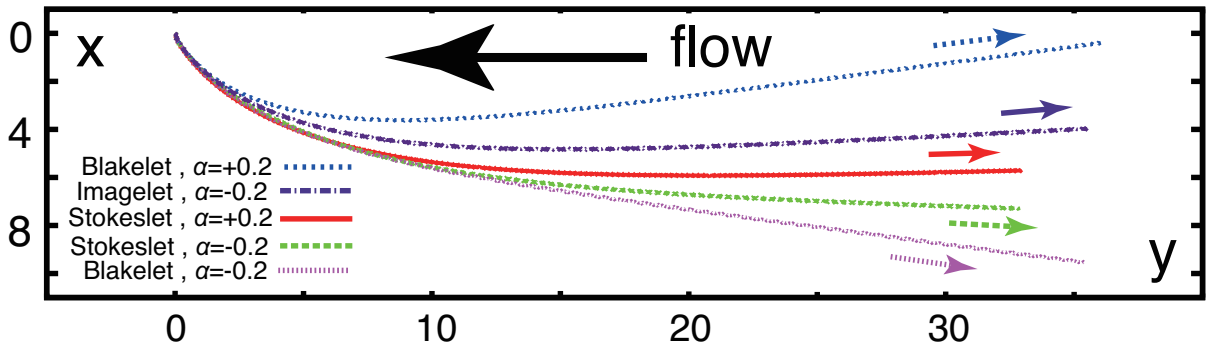

Figure 2: The effect of shear on computed sperm trajectories in a background flow with a surface repulsion potential, specified by the parameters of Table 2. The virtual sperm has a symmetric flagellar envelope, $\Gamma = \infty$, with $\alpha = -0.2$, corresponding to human sperm chirality, or $\alpha = +0.2$, corresponding to the opposite chirality found in mouse, whilst the initial attack angle is $\theta_{init} = 0.2\pi$ and the sperm is initially located at $\boldsymbol{X}(s = 0, t = 0) = (0, 0, 0.1)$. Other parameters are given in Table 1. Given the initial conditions, we are observing virtual sperm behaviour in the vicinity of the origin of the repulsive surface potential at $z = 0$ and the trajectories are presented in terms of their projection onto the x-y plane, thus representing paths that would be observed in the focal plane of a microscope when viewed from above. The trajectory labelled *Blakelet* gives the predicted path of this sperm near a no-slip surface, whereas the trajectory labelled *Imagelet* is the prediction for this sperm near a surface of fixed tangential stress and no normal velocity. The predictions for the *Stokeslet* correspond to the absence of hydrodynamic wall effects, though the surface repulsion potential is still included in the model.

3 Results

In all the presented results below the mass, length and time units are such that the non-dimensional viscosity, flagellum length and frequency are of unit value.

3.1 Elliptical Helicoid Beating In Shear Flow Near and Distant from Surfaces

We first of all consider the effects of shear for a virtual sperm with the same flagellar chirality as human, which is of opposite parity to that of mouse. Hence the flagellar parameters are given by Table 1 with the waveform parameters $\alpha = -0.2$, $\Gamma = \infty$, with the latter imposed to ensure a symmetric beat pattern, as specified by equation (2.1). The shear flow is given by equations (2.4), (2.5), with parameters as in Table 2.

The Blakelet solution for a no-slip surface at $x_3 \equiv z = 0$ exhibits boundary accumulation and rheotaxis, whereby the virtual sperm swims into the flow, as observed in Fig 2. There is also a transverse velocity, in the same direction as the predictions and observations of Kantsler et. al. [16]. Furthermore the direction of the transverse velocity changes with chirality parity, as seen in Fig 2, and this switch is also observed in the presence of a flat surface with specified tangential stress, corresponding to the *Imagelet* solution.

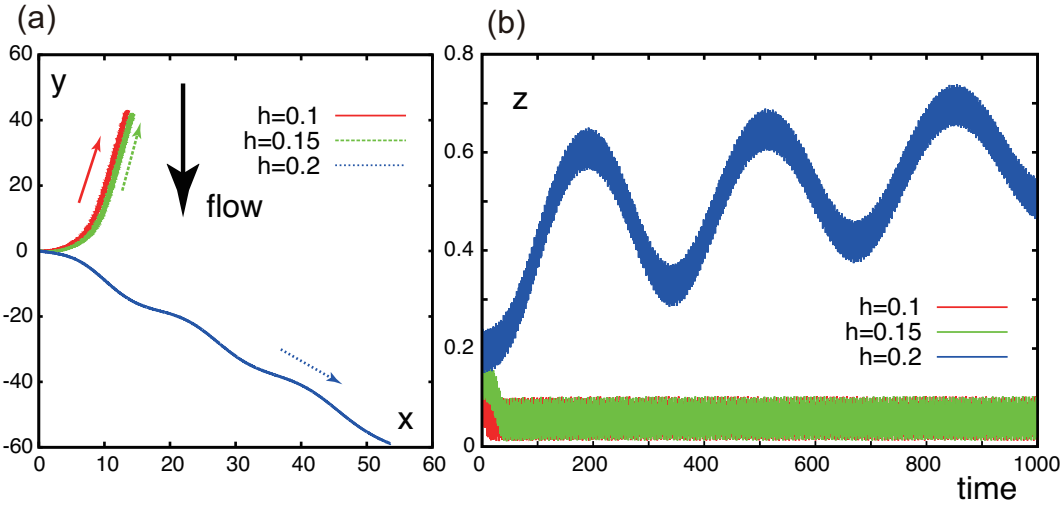

Figure 3: The influence of the surface on computed sperm trajectories in a background flow and surface repulsion potential, specified by the parameters of Table 2. (a) A virtual sperm in the presence of a no-slip surface is considered with sperm parameters values given in Table 1 and also that $\Gamma = \infty$, $\alpha = -0.2$, $\theta_{init} = 0$, $X(s = 0, t = 0) = (0, 0, h)$. The projection of the trajectory onto the plane of the no-slip surface is plotted for this sperm with the arrow showing the direction of swimming for different non-dimensional starting heights, h, above the no-slip surface. (b) A further breakdown of this virtual sperm's trajectory, with plots of z, its distance from the no-slip surface, as a function of time for different starting heights above the no-slip surface.

In Fig. 2 projected trajectories are also presented for the Stokeslet solution, which corresponds to the absence of hydrodynamic surface interactions from the boundary conditions on the flat plane. The repulsive surface potential, equation (2.5), which is due to many factors such as van der Waals forces but *not* hydrodynamics, is taken into consideration and, due to the cell rotation arising from the elliptical helicoid beat pattern, the virtual sperm oscillates in and out of the region of influence of this potential (as also observed in Fig. 3b), confining it to a region of low shear flow. Rheotaxis in the x-y plane is also observed, emphasising that a surface hydrodynamic interaction is not required for rheotaxis, as described in Kantsler et al.'s minimal model, though restriction to regions of sufficiently low flow is required.

Furthermore in Fig 3 we consider further simulations of the virtual sperm with $\alpha = -0.2$, corresponding to the chirality of human sperm, but now with variation in the initial distance from the no-slip surface, denoted h. We see that once this initial distance reaches 20% of the flagellum length, $h = 0.2$ which is about 11 microns for human sperm, boundary accumulation is lost and the sperm is swept downstream without a discernible rheotaxis as it enters the bulk, faster, flow with increasing z. Hence we see that constraining the sperm to remain in a low flow region is an important feature of rheotaxis and this can be achieved by boundary accumulation.

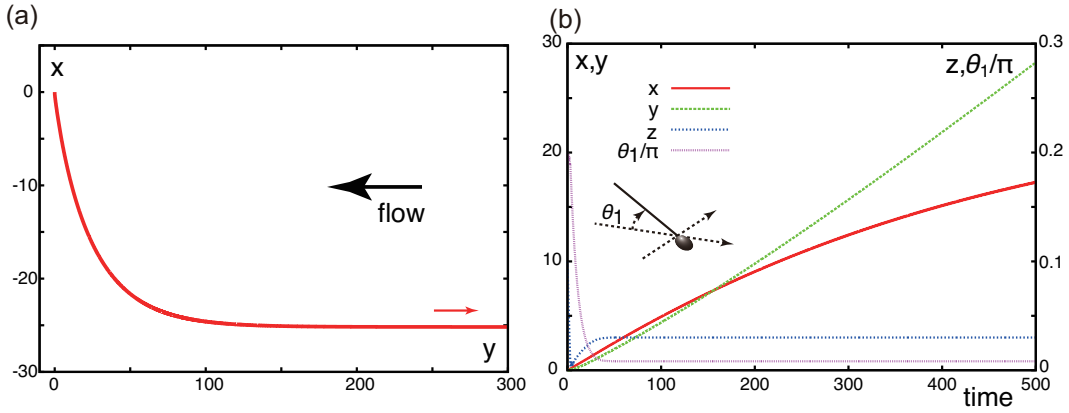

Figure 4: Planar swimming sperm dynamics in a background flow and surface repulsion potential, specified by the parameters of Table 2. (a) A virtual sperm in the presence of a no-slip surface is considered with sperm parameter values of Table 1, and the further specification with $\Gamma = \infty$, $\alpha = 0$, $\theta_{init} = 0.2\pi$ and the sperm is initially located at $\boldsymbol{X}(s = 0, t = 0) = (0, 0, 0.1)$. The projection of the trajectory onto the plane of the no-slip surface is plotted for this sperm with the smaller arrow showing the direction of swimming. (b) A further breakdown of this virtual sperm's trajectory, with plots of x, y, z as a function of time together with θ_1, its angle of attack relative to the no-slip surface, that is the angle between the ξ_3 axis and the no slip surface $z = 0$. The sperm head in the figure is solely for illustration of the definition of the angle and has not been considered in the modelling.

3.2 Planar Beating In Shear Flow Near a No-Slip Surface

We proceed to consider sperm swimming in a shear flow near a no-slip surface at $x_3 \equiv z = 0$ with a planar flagellar beat. We have a virtual human sperm with a symmetric flagellar waveform given by equation (2.1), using the parameters of Table 1 with a flagellar length $L = 56\mu$m and waveform parameters $\alpha = 0$, $\Gamma = \infty$. In particular $\alpha = 0$ ensures the flagellar waveform is the projection of an elliptical helicoid beat onto the plane containing its axis of symmetry. The shear flow and repulsion forces are given by equations (2.4), (2.5), respectively with the parameters specified in Table 2. In Fig 4a, one can observe that this planar beating virtual sperm also rheotaxes into the direction of the flow and thus chirality is not necessary for rheotaxis. Furthermore, the planar beater trajectory has no transverse velocity for asymptotically long time and also possesses a larger radius of curvature at intermediate times, consistent with observations that the trajectories of sperm with nearly planar beats have reduced curvature [16]. From Fig 4b, we also predict that the simulated virtual sperm boundary accumulates very close to the no-slip surface, at a height of $\approx 0.03L \sim 1.7\mu$m, with a tiny angle of attack, so that the possession of a flagellum elevated into the shear flow, as with elliptical helicoid beaters, is again not a necessary feature of rheotaxis.

3.3 Asymmetric Flagellar Beating In Shear Flow Near a No-Slip Surface

Finally, we explore the impact of flagellar waveform asymmetry on rheotaxis in shear flows with a no slip boundary at $x_3 \equiv z = 0$. We consider a virtual sperm possessing an asymmetric flagellar waveform, given by equation (2.2) with the chirality parameter α specified in Fig 5 and the radius

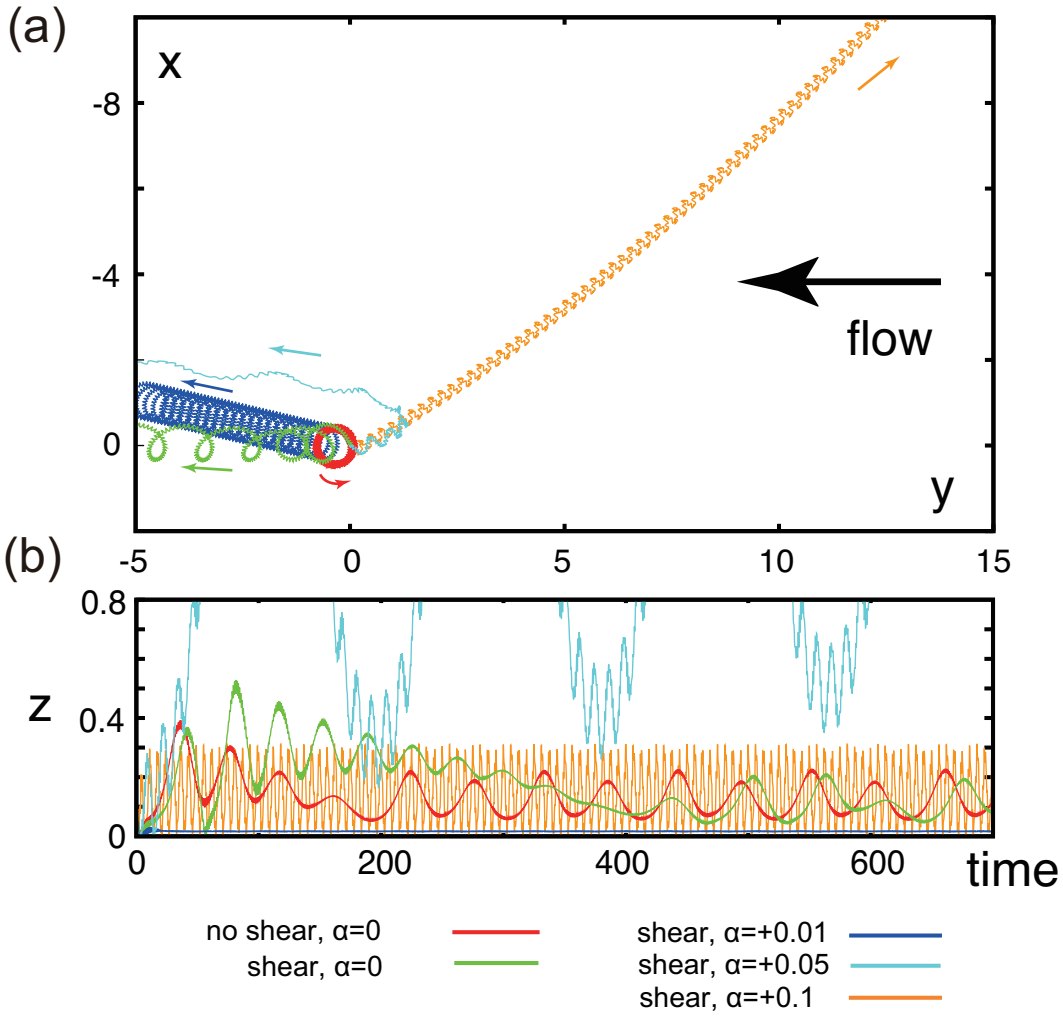

Figure 5: The impact of an asymmetric flagellar waveform for a sperm swimming in a background flow and surface repulsion potential, specified by the parameters of Table 2, with a no-slip surface at $z = 0$. For all trajectories the parameters are given by Table 1 with α as specified, $\Gamma = 0.5$, $\theta_{init} = 0.2\pi$ and the initial location $\boldsymbol{X}(s = 0, t = 0) = (0, 0, 0.1)$. The exception is the red trajectory, for which there is no background flow. (a) The projection of the trajectories onto the plane of the no-slip surface. (b) Time course of the height z of the flagellum above the surface, as measured from the origin of the flagellar frame.

of curvature of the flagellar waveform, Γ, equal to 0.5. The shear flow and repulsion forces are those used previously and given by equations (2.4), (2.5), respectively with the parameters of Table 2, except for trajectories in the absence of shear, for which the shear strength, $\dot{\gamma}$, is zero. In Fig 5(a), the trajectories associated with asymmetric waveform swimmers are projected onto the no-slip plane, whereas a sideview of these trajectories is presented in Fig 5(b).

In the absence of shear and chirality, the virtual sperm has a planar asymmetric wave associated with a sea urchin beat pattern. In Fig 5(a),(b) its trajectory is presented in red and one can observe that this sperm boundary accumulates and executes tight swimming circles with a diameter on the scale of a

cell length, consistent with observations which range from 25 microns [33] to roughly 100 microns [21], depending on experimental details. On introducing a shear flow, the resulting trajectory is plotted in green; one can observe that boundary accumulation is not disrupted, even if the transients are different, and that the swimming turning circles persist, though the sperm is slowly swept downstream at a rate of about 0.02 cell lengths per beat cycle.

Introducing a small chirality, with $\alpha = +0.01$ for the navy trajectory in Fig 5, induces no substantial effect; the virtual sperm still boundary accumulates, albeit *much* closer to the surface, with $z \approx 0.02$, and executes turning circles with a slow downstream drift of about ≈ 0.005 cell lengths per beat cycle, due to the smaller shear velocity at the boundary accumulation height. A small, chirality induced, transverse drift velocity to the flow is predicted and, as detailed in Section 4 of the *Supplementary Information*, once non-trivial flagellar chirality is present the direction of rotation near the no-slip surface is dictated by the sign of the chirality via boundary accumulating behaviours.

These predictions are consistent with observations of many marine sperm, such as sea urchin and *Ciona*, which exhibit circling trajectories with a single rotation direction [34, 26, 21], determined by the sign of the flagellar chirality [13] which is counter-clockwise when viewed from above for a positive chirality [34]. Furthermore, whilst the predicted slow downstream drift is not explicitly observed in the shear flow experiments of Miki and Clapham [21] such effects would be difficult to discern in the duration of these experiments as, for example, the sperm execute less than a single revolution and the magnitude such effects would also be contingent on the quantitative details, such as the boundary accumulation height.

With further increases in chirality, with $\alpha = +0.05$ as depicted in cyan in Fig 5, boundary accumulation is lost and the virtual sperm is swept downstream. This emphasises how the presence or absence of rheotaxis near a surface inherits a subtle dependence on the waveform, associated with the presence or absence of boundary accumulation. Finally, as reported in Section 4 of the *Supplementary Information* larger magnitudes of chirality induce a relatively progressive sperm motility. Such a virtual sperm does not exhibit a highly curved path in the absence of flow and, when subjected to shear flow, rheotaxis is predicted to occur once boundary accumulation is also present, as illustrated in Figure 5 for $\alpha = 0.1$.

More generally, these observations of virtual sperm emphasise that rheotaxis requires sperm to persist in regions of relatively low shear, so that they are not swept away, and the predictions for the absence of rheotaxis in sperm with highly asymmetric flagellar waveforms is consistent with simply whether the flagellar asymmetry induces an angular velocity that dominates rheotactic-induced turning, or vice-versa.

4 Discussion and conclusions

We have theoretically considered sperm swimming in a background shear flow to explore the prospects for rheotaxis, the directed bias of sperm swimming by the flow together with the potential requirements for this guidance cue to be observed, using an elliptical helicoid flagellar beating given that recent experimental studies have focussed on this beat pattern [21, 16]. In our validation studies in the absence of a background flow, as presented in the *Supplementary Information*, we have observed that sperm with this beat pattern typically boundary accumulate with a significant trajectory curvature for the beat-period averaged path near a no-slip surface. In particular, this mode of boundary

accumulation differs from the hydrodynamic boundary capture theoretically explored in [14, 15] and much of [28], where the repulsive surface potential was not taken into consideration. Thus we often work in the regime where the virtual cell reaches far closer to the surface, so that shear does not wash the cell downstream, and hence the accumulation heights in this study, which generally satisfy $h < 0.05L$, are much smaller than that predicted by simply the hydrodynamic interaction of the cell and the boundary, in the absence of a surface repulsion potential.

The trajectory curvature of the boundary accumulated cell can be readily understood. For an elliptical helicoidal beat pattern, there is greater viscous drag on the flagellum nearer a no-slip surface in total, over a whole beat cycle, generating a net viscous torque about the z axis. As the cell must be torque free, this drag is compensated by the torques induced by an angular velocity of the cell about the z axis; hence the trajectory curves in the x-y plane. In contrast, the planar swimmer near a surface will possess a very small angle of attack as seen in Fig 4b, and previous work [28, 15] and thus this effect will be negligible, leading to effectively no trajectory curvature as seen in simulations [28, 15] and experiments [29]. Furthermore, in the presence of a flat surface with a fixed tangential stress, which is zero if there is no background shear flow, there is less viscous drag for motion parallel to the boundary, and thus the trajectory curvature is in the opposite direction, as confirmed both theoretically and experimentally for bacteria [8], which also swim with rotation. Similarly, by this mechanism one has that changing the chirality parity of the flagellar wave changes the directions of the torques and thus the direction of the surface induced trajectory curvature.

In the presence of shear flow $\boldsymbol{u}^{\infty} = -\dot{\gamma} z \mathbf{e}_2$, which is sufficiently weak to allow sperm to swim against the current if they stay within the vicinity of $z = 0$, rheotactic guidance is observed, with the virtual sperm turning into the flow which is compatible with observations [21, 16]. The fact the bias in the trajectory to turn into the flow is identical both near a no-slip surface and a flat surface of fixed tangential stress rules out a trajectory curvature via surface interaction torques and also shows that the latter is negligible compared to torques induced by rheotaxis for a sperm that is not aligned with the background flow. Nonetheless, the predicted transverse velocity is of opposite sign on comparing a flat, tangential stress surface and a no-slip surface, indicating that this specific aspect of the rheotactic phenomenon is related to surface hydrodynamic effects. The direction of the transverse velocity once rheotaxis into the flow has been established is consistent with simply the superposition of surface induced trajectory curvature with, for example, a switch in the transverse velocity direction on changing the sign of the flagellar waveform chirality. The surface trajectory curvature is not the only effect in that a smaller chiral-dependent transverse velocity is predicted to persist even for the *Stokeslet* solution in the absence of hydrodynamic surface-interactions, though the virtual sperm is constrained near $z = 0$ because of the repulsive surface potential which is due to many factors, such as van der Waals forces. Thus, we predict that surface interactions dominate the transverse velocity associated with the rheotaxis of an elliptical helicoid swimmer, though chirality-dependent corrections are also present; furthermore, an analytical model rich enough to include rheotaxis and the contrasting influence of different surfaces and chirality in particular requires an extension of existing modelling frameworks.

We also note that rheotaxis is predicted to occur even when the sperm is not in the vicinity of a surface, as long as the sperm is confined in a region where the background flow is insufficient to wash the sperm away, as implicit in Kanstler et al.'s minimal model [16]. In particular, the *hydrodynamic* interaction of a surface and the sperm is not required, as highlighted by the Stokeslet solutions of Fig 2 where, via the surface repulsion potential, the sperm is constrained to remain in a region with sufficiently low shear flow to prevent washout. This reasoning would indicate that rheotaxis can occur in the bulk, as

observed for bacteria [20], but with the simple shear flows typically considered in experimental and theoretical investigations of sperm one simply has washout, unless the sperm persists in the region of low shear close to the boundary. In particular, within confining geometries, such as microdevices or the female reproductive tract, rheotactic directed guidance in the bulk is not inconsistent with the current study, as the flow does not increase indefinitely away from boundaries.

Furthermore a virtual planar beater will rheotax without a large angle of attack into a surface highlighting that the planar beat patterns of boundary accumulating human sperm in viscous media do not preclude rheotaxis, and more generally that rheotaxis need not be as sensitive to the flagellar waveform as suggested in earlier studies [21]. In particular, chirality and a significant angle of attack relative to a surface are not mechanically required. Nonetheless, we have also observed predictions that an asymmetric beat with tight circling is sufficient to prevent rheotaxis, consistent with observations that sea urchin and CatSper mutant sperm do not rheotax. The mechanical explanation for this is simple. A shear flow induces a torque on a swimmer unless it is already aligned with the flow, as illustrated in Kantsler et al's minimal model [16]. If this is the dominant torque due to the flagellar dynamics the trajectory will possess a curvature generating a compensating torque, so that the cell is torque-free as required in the inertialess limit, which induces the rheotactic response causing the swimmer to align with the flow. However if the torques on the flagellum are dominated by another aspect of the flagellar motion, such as asymmetry, the compensating torque governing the flagellar trajectory will predominantly compensate *this* dominating feature, rather than the shear flow induced torque, subordinating a rheotactic response.

In summary, we have the simple prediction that rheotaxis requires (i) a confining influence to prevent sperm reaching flow rates that will sweep them away typically, but not necessarily, a boundary or a confined geometry and (ii) in the no-flow scenario, an absence of sperm circling that would subordinate the rheotactic response. This is a much weaker set of requirements than originally proposed for sperm [21] and is consistent with all modelling results presented here and previous observations, in turn suggesting that rheotaxis may be even more prevalent as a guidance mechanism.

We reconsider the planar beating sperm in view of these criteria. Let U denote its swimming speed, H denotes its boundary accumulation height and we assume this is not significantly altered by the presence of a shear flow $\boldsymbol{u}^\infty = -\dot{\gamma} z \mathbf{e}_2$ and also that boundary accumulation is the only means by which sperm can be constrained to low shear-flow regions. Then the above conditions for rheotaxis near a surface are

$$\dot{\gamma} \ll U/H, \qquad R_{rheo} \ll R_{turn}, \tag{4.1}$$

where R_{rheo} is the radius of curvature of the trajectory associated with the initial rheotactic response and R_{turn} is the radius of curvature associated with the shear-flow free swimming. From our simulation of a planar beater, Fig 4a, we find $R_{rheo} \approx 40L$; assuming the rheotactic trajectory curvature, R_{rheo}^{-1}, has a linear dependence on the shear rate, as observed in the calculations of Kantsler et. al. [16], we have $R_{rheo} \approx 4L\omega/\dot{\gamma}$, where the frequency dependence is required on the grounds of dimensional consistency. Defining a non-dimensional rheotactic number, $\mathcal{R}$ and a non-dimensional shear rate, $\mathcal{S}$, by

$$\mathcal{R} := \frac{U R_{turn}}{L\omega H}, \qquad \mathcal{S} := \dot{\gamma}\frac{R_{turn}}{\omega L} \tag{4.2}$$

we have from the conditions (4.1) the prediction that $\mathcal{R} \gg 4$ is a necessary condition for rheotaxis, in which case rheotaxis will manifest on increasing shear rates once $\mathcal{S} \gg 4$.

Similarly for the elliptical helicoid beating, with analogous assumptions, we find $\mathcal{R} \gg 1$ is a necessary condition for rheotaxis, which will occur on increasing shear rates once $\mathcal{S} \gg 1$. The non-dimensional factors that differ between the planar beater and the elliptical helicoid beat arise from inspecting the numerical predictions for R_{turn} and thus will certainly differ according to detailed beat pattern and other complexities, such as the sperm head shape; as such these conditions for rheotaxis are crude order of magnitude estimates. Nonetheless, when the rheotactic number $\mathcal{R}$ is sufficiently large it is predicted that rheotaxis can occur, at least for an appropriate choice of shear rate.

For illustration we demonstrate in Section 5 of the *Supplementary Information* that the lack of sea urchin sperm surface rheotaxis in experiments [21] is predicted by the rheotactic conditions; analogous deductions are presented for CatSper mutants. This analysis in the *Supplementary Information* proceeds to consider the above rheotactic criteria for star-spin hyperactivated human sperm [23], which are predicted to fail to rheotax. In contrast, for the hyperactivation of mouse sperm in viscous solution, where essentially straight line swimming becomes manifest [21], the potential for sperm rheotaxis is indicated, at least given boundary accumulation, though in this experimental study it is also difficult to estimate the turning circle of these sperm for more precision. The requirement for boundary accumulation however is counter-indicated in previous simulations of hyperactivated sperm [15] though geometrical confinement may also be relevant for a rheotactic response. Nonetheless this latter caveat also highlights that the complexities of boundary accumulation, such as a flagellum wavenumber dependence [28, 15], are implicitly inherited by the criteria for boundary accumulating rheotaxis via the accumulation height, H.

In summary, we have explored the rheotactic response of virtual sperm via a detailed simulation study, using a sperm model of a prescribed planar, or ellipsoidal helical, waveform and a negligibly small sperm head. This virtual sperm typically rheotaxes in shear flow, turning into the upstream direction. In practice boundary accumulation is required to confine the sperm to a region of sufficiently small flow so as to prevent washout, though the actual interactions between the virtual sperm and the boundary are subordinate to the rheotactic response. Nonetheless, these interactions induce a small transverse velocity perpendicular to the flow direction once rheotaxis is established for non-planar waveforms. In contrast tightly circling swimming sperm, due to asymmetric flagellar waveforms, do not rheotax as the torques due to the asymmetric waveform dominate the directionality of the sperm trajectory. Hence we have suggested that rheotaxis requires confinement, simply to prevent washout, and a sufficiently weak circling swimming trajectory in the absence of flow, with order of magnitude constraints for the realisation of rheotaxis via boundary accumulating confinement. These latter constraints explain previous observations [21, 16], as well as our own simulation results, suggesting that rheotaxis can readily achieve sperm guidance across many different species providing the flagellar waveform is not significantly asymmetric and the cell boundary accumulates, or otherwise remains within regions of relatively low flow.

Acknowledgements

KI acknowledges JSPS for its fellowship and KAKENHI, grant-in-aid for a JSPS Fellow. Elements of these simulations were performed using the cluster within the Research Institute for Mathematical Sciences (RIMS), Kyoto University.

References

[1] Alvarez L, Friedrich BM, Gompper G, Kaupp UB. 2014, The computational sperm cell. *Trends Cell Biol.*, **24**, 198–207.

[2] Bahat A, Eisenbach M. 2006, Sperm thermotaxis. *Mol. Cell. Endocrinol.*, **252**, 115–119.

[3] Blake JR. 1971, A note on the image system for a stokeslet in a no slip boundary. *Proc. Camb. Phil. Soc.*, **70**, 303–310.

[4] Bretherton FP, Rothschild. 1961 Rheotaxis of spermatozoa, *Proc. Roy. Soc. Lond. B*, **153**, 490–502.

[5] Cosson J. (Editor) Flagellar movement and sperm guidance. *Bentham Publishers*, 2015.

[6] Cortez R. 2001, The method of regularized stokeslets. *SIAM J. Sci. Comput.*, **23** 1204–1225, 2001.

[7] Croxatto HB. 2002, Physiology of gamete and embryo transport through the fallopian tube. *Reprod. Biomed. Online*, **4** 160–169.

[8] DiLeonardo R, Dell'Arciprete D, Angelani L, Iebba V. 2011, Swimming with an Image. *Phys. Rev. Lett.*, **106**, 038101.

[9] Elgeti J, Kaupp UB, Gompper G. 2010, Hydrodynamics of sperm cells near surfaces. *Biophys. J.*, **99**, 1018–1026.

[10] Gillies E, Cannon RM, Green RB, Pacey AA. 2009, Hydrodynamic propulsion of human sperm. *J. Fluid Mech.*, **625**, 445–474.

[11] Ishijima S, Oshio S, Mohri H. 1986, Flagellar movement of human spermatozoa. *Gamete Res.*, **13** 185–197.

[12] Ishijima S, Hamaguchi MS, Naruse M, Ishijima SA, Hamaguchi Y. 1992, Rotational movement of a spermatozoon around its long axis. *J. Exp. Biol.*, **163**, 15–31.

[13] Ishijima S, Hamaguchi Y. 1992, Relationship between direction of rolling and yawing of golden hamster and sea urchin spermatozoa. *Cell Struct. Funct.*, **17**, 319–323.

[14] Ishimoto K, Gaffney EA. 2013, Squirmer dynamics near a boundary. *Phys. Rev. E*, **88**, 062702.

[15] Ishimoto K, Gaffney EA. 2014, A study of spermatozoan swimming stability near a surface. *J. Theor. Biol.*, **360**, 187–199.

[16] Kantsler V, Dunkel J, Blayney M, Goldstein RE. 2014, Rheotaxis facilitates upstream navigation of mammalian sperm cells. *eLife*, **3**, e02403.

[17] Klein JD, Clapp AR, Dickinson RB. 2003, Direct measurement of interaction forces between a single bacterium and a flat plate. *J. Colloid Interface Sci.*, **261**:379–385.

[18] Kölle S, Dubielzig S, ReeseS, Wehrend A, König P, Kummer W. 2009, Ciliary transport, gamete interaction, and effects of the early embryo in the oviduct: ex vivo analyses using a new digital videomicroscopic system in the cow. *Biol. Reprod.*, **81**, 267–274.

[19] Lott G. 1872, *Zur Anatomie und Physiologie des Cervix uteri*, Ferdinand Enke, Stuttgart, Germany.

[20] Marcos, Fu HC, Powers TR, Stocker R. 2012, Bacterial rheotaxis. *Proc. Natl. Acad. Sci. U.S.A.*, **109**, 4780-4785.

[21] Miki K, Clapham DE. 2013, Rheotaxis guides mammalian sperm. *Curr. Biol.*, **23**, 443–452.

[22] Ralt D, Manor M, Cohen-Dayag A, Tur-Kaspa I, Ben-Shlomo I, Makler A, Yuli I, Dor J, Blumberg S, Mashiach S, Eisenbach M. 1994, Chemotaxis and chemokinesis of human spermatozoa to follicular factors. *Biol. Reprod.*, **50**, 774–785.

[23] Robertson L, Wolf DP, Tash JS. 1988, Temporal changes in motility parameters related to acrosomal status - identification and characterization of populations of hyperactivated human sperm. *Biol. Reprod.*, **39**, 797–805.

[24] Pozrikidis C. 1992, *Boundary Integral and Singularity Methods for Linearized Viscous Flow*. Cambridge University Press.

[25] Roberts AM. 1970. Motion of spermatozoa in fluid streams, *Nature*, **228**, 375–376.

[26] Shiba K, Baba SA, Inoue T, Yoshida M. 2008, Ca^{2+} bursts occur around a local minimal concentration of attractant and trigger sperm chemotactic response. *Proc. Natl. Acad. Sci. U.S.A.*, **105**, 19312–19317.

[27] Smith DJ, Blake JR. 2009. Surface accumulation of spermatozoa: a fluid dynamic phenomenon. *Math. Sci.*, **34** 74–87.

[28] Smith DJ, Gaffney EA, Blake JR, Kirkman-Brown JC. 2009 Human sperm accumulation near surfaces: a simulation study. *J. Fluid Mech.*, **621**, 289–320.

[29] Smith DJ, Gaffney EA, Gadêlha H, Kapur N, Kirkman-Brown JC. 2009, Bend propagation in the flagella of migrating human sperm, and its modulation by viscosity. *Cell Motil. Cytoskel.*, **66**, 220–236.

[30] Spagnolie SE, Lauga E. 2012, Hydrodynamics of self-propulsion near a boundary: predictions and accuracy of far-field approximations. *J. Fluid Mech.*, **700**, 105–147.

[31] Ward GE, Brokaw CJ, Garbers DL, Vacquier VD. 1985. Chemotaxis of Arbacia-Punctulata spermatozoa to resact, a peptide from the egg jelly layer. *J. Cell Biol.*, **101**, 2324–2329.

[32] Winet H, Bernstein GS, Head J. 1984, Observations on the response of human spermatozoa to gravity, boundaries and fluid shear. *J. Reprod. Fert.*, **70**, 511–523.

[33] Woolley DM, Vernon GG. 2001, A study of helical and planar waves on sea urchin sperm flagella, with a theory of how they are generated. *J. Exp. Biol.* **204**, 1333-1345.

[34] Woolley DM. 2003, Motility of spermatozoa at surfaces. *Reproduction*, 126, 259–270.

[35] Zimmer RK, Riffel JA. 2011, Sperm chemotaxis, fluid shear, and the evolution of sexual reproduction *Proc. Natl. Acad. Sci. U.S.A.*, **108**, 13200–13205.

Supplementary Information

Fluid flow and sperm guidance: a simulation study of hydrodynamic sperm rheotaxis

Kenta Ishimoto[1,2*] and Eamonn A. Gaffney[3†]

[1] The Hakubi Center for Advanced Research, Kyoto University, Kyoto, 606-8501, Japan
[2] Research Institute for Mathematical Sciences, Kyoto University, Kyoto, 606-8502, Japan
[3] Wolfson Centre for Mathematical Biology, Mathematical Institute, University of Oxford, Oxford OX2 6GG, UK

1 Parameter estimation

We detail the motivation for the parameter estimates used in Tables 1, 2 of the main text, which are recapitulated here for convenience in Supplementary Information Table 1.

The flagellar length L and the beat frequency T^{-1} are those of uncapacitated human sperm [8]. The predicted sperm trajectory is independent of the viscosity of the surrounding medium, μ, as the mass-scale does not enter the mapping between non-dimensional and dimensional trajectories and hence a viscosity estimate is not presented, though it must be such that the sperm flagellar waveforms used in this study are reasonable. The parameter α governs the flagellum wave chirality and a selection of values are considered, with $\alpha = 0$ constituting a planar waveform, $\alpha > 0$ a right handed helix as found in mouse [38] and $\alpha < 0$ gives a left handed helix, as observed for human sperm with $\alpha = -0.2$ [16, 17]. The parameter Γ controls the level of flagellar wave asymmetry, with infinite Γ corresponding to a symmetric flagellum whilst $\Gamma/L = 0.5$ gives circular swimming trajectories with a diameter of roughly the flagellum length, L, in Fig. 5 of the main text whilst sea urchin with asymmetric flagella waveforms have been observed to execute circles with diameters as small as 25 microns [37] or approximately 100 microns [23], depending on experimental details. The parameters k, B further describe the flagellar waveform, and the parameter estimates given are those of Dresdner and Katz [8], though in general these parameters are variable; finally the flagellar radius is based on images of the human sperm proximal flagellum, indicating a radius of approximately 500nm, though we do not consider the geometry of the tapering outer dense fibres found in mammalian sperm [11, 13].

*ishimoto@kurims.kyoto-u.ac.jp
†gaffney@maths.ox.ac.uk

Parameter	Interpretation	Value
L	Flagellar length	56μm
$1/T = \omega/[2\pi]$	Beat frequency	14 Hz
α	Chirality parameter	$\pm\{0, 0.01, 0.05, 0.1, 0.2\}$
Γ/L	Asymmetric waveform parameter	$\{0.5, \infty\}$
kL	Wavenumber	3π
B	Flagellar envelope parameter	$0.2L$
a	Flagellar radius	$0.01L$
$\dot{\gamma}$	Background shear flow strength	$0.1T^{-1}$
g/μ	Repulsion potential magnitude	$10LT^{-1}$
d	Repulsion potential lengthscale	$0.005L$

Table 1: Supplementary Information Table 1. Reference parameter values for the flagellum waveform, the shear flow strength and the repulsive surface potential.

To consider the shear flow strength, recall that $\boldsymbol{x} = (x_1, x_2, x_3) \equiv (x, y, z)$ are coordinates in the laboratory reference frame, and that the boundary where the repulsive surface potential is imposed corresponds to $z = 0$. Then, the extent of shear is given by $\dot{\gamma}$ and defined via the background flow velocity vector field, $\boldsymbol{u}^{\infty}(\boldsymbol{x}) = -\dot{\gamma} z \mathbf{e}_2$. The fact $\dot{\gamma}T$ is small indicates that we are considering a relatively weak shear flow relative to the velocity scales of sperm swimming at cell lengthscales away from $z = 0$, as generally required to prevent sperm washout from the system. The parameter g is the magnitude of the assumed repulsive surface forces at $z = 0$. Its scaling with viscosity, μ, is for convenience – we simply take g to be sufficiently high to ensure sperm do not crash into the boundary at $z = 0$; this is consistent with human sperm behaviour in glassware experiments once dilute human serum albumin is present in the media, which prevents sperm colliding with and sticking to the glassware [28].

Finally, the parameter $d = 0.005L = 280$nm is a measure of the repulsion potential decay length, which is larger than the measured scale of 50nm for bacteria [22], but the details close to the surface are qualitative only as the surface potential varies with the cell, solutes and surface and is not documented for sperm. The impact of variation in d on the quantitative details of trajectory curvatures is briefly presented in Fig 2d below, which shows that d influences trajectory curvatures, though not the qualitative details. Thus such uncertainty in the surface potential represents a source of modelling uncertainty which mitigates against the additional computational expense of including virtual sperm heads in the modelling. Further justification for this particular approximation follows in the next section.

2 Justifying the neglect of the sperm head

For sperm, the head is relatively small compared to the lengthscale of the flagellum and so we consider the errors associated with neglecting the head in calculating sperm trajectories, especially their curvature and thus the impact of rheotactic guidance cues.

For a small amplitude resistive force theory calculation, with a tangential resistance coefficient C_T, a spherical sperm head of lengthscale q and a flagellar wavenumber, k, head effects induce a correction

in the swimming speed at the order of [15]

$$\frac{6\pi q}{C_T L} = \frac{3q}{L}\left[\log\left(\frac{4\pi}{ak}\right) - \frac{1}{2}\right] \approx 8.1\frac{q}{L} \approx 0.2,$$

given the parameter values of Table 1 and $q \sim 1.6\mu$m, which is representative of human sperm.

We proceed to consider the scale of the head torque to the scale of the flagellum torque. Let $\boldsymbol{X}(s,t)$ denote the location of the flagellum at time t and arclength $s \in [0, L]$, and $\boldsymbol{F}$ denote the viscous drag per unit arclength at this location. Then the torque ratio is of the order of

$$\frac{8\pi\mu q^3\Omega}{|\int_0^L \boldsymbol{X} \wedge \boldsymbol{F}\mathrm{d}s|} \sim \frac{8\pi\mu q^3\Omega}{\frac{L}{2}C_T U L} \sim \frac{16\pi\mu q^3\Omega}{C_T U L^2} \sim \frac{8q^3\Omega}{UL^2}\left[\log\left(\frac{4\pi}{ak}\right) - \frac{1}{2}\right] \approx \frac{22q^3}{L^3}\frac{\Omega L}{U}.$$

For a trajectory with radius of curvature r_c, with T_c the time for a complete revolution if the angular velocity and translational velocities were fixed, one has $\Omega \sim 2\pi/T_c$ and $U \sim [2\pi r_c]/T_c$ so that $\Omega/U \sim 1/r_c$. For the tightest turning circle we consider in the results section of the main text $r_c \sim L/2$ whence the ratio of toque scales becomes

$$44\frac{q^3}{L^3} \approx 10^{-3}.$$

Hence the head torque scale is three orders of magnitude smaller than the flagellum torque scale, essentially as the ratio of head to flagellar torques scales with the cube of q/L rather than linearly, and thus head torques are subordinate and can be neglected.

Hence neglecting the sperm head entails that angular velocities are generally accurate and linear velocities are of the correct scale; further the linear velocity is always overestimated and hence the trajectory curvature underestimated. Thus neglecting the sperm head gives the correct scale of the rheotactic effect with a relatively small underestimation error motivating the neglect of the head, especially given quantitative accuracy is not feasible due to the modelling uncertainties associated with the parameter estimation of the repulsive surface potential.

3 The numerical algorithm and its validation

In this section, the numerical methods and algorithms are documented, together with modelling validation, including primary simulations for elliptical helicoidal beating sperm near a no-slip surface in the absence of background flow.

3.1 Numerical schemes

As spermatozoa are small enough to neglect inertia, the flow around the cell obeys Stokes' equations, which can be solved to within asymptotically small errors using the regularized Stokeslet method (RSM), as first developed by Cortez [6], though our implementation is analogous to that used in Gillies et al.'s computational study of human sperm [14].

The RSM method requires the regularized Stokeslet, which is a fundamental solution of Stokes' equations for an external force localised to within a lengthscale of ϵ of the point $\boldsymbol{x}_0$. There is not

a unique choice but a standard one is that the force at location $\boldsymbol{x}$ is given by $\boldsymbol{F}\psi_\epsilon(\boldsymbol{x},\boldsymbol{x}_0)$, with $\boldsymbol{F}$ constant, $\psi_\epsilon = 15\epsilon^4(r^2+\epsilon^2)^{-7/2}/8\pi$, $r = |\boldsymbol{x}-\boldsymbol{x}_0|$ and, with L denoting the flagellum length, ϵ is the regularisation lengthscale, with ϵ/L the parameter governing the asymptotic accuracy of the method.

In this instance, the regularized Stokeslet is given by

$$ {}^{\epsilon}G^S_{ij}(\boldsymbol{x}-\boldsymbol{x}_0;\epsilon) = \frac{(r^2+2\epsilon^2)\delta_{ij}+r_ir_j}{(r^2+\epsilon^2)^{3/2}}. \tag{3.1}$$

In presence of a rigid no-slip infinite plane wall, the regularized Stokeslet can be constructed by introducing additional localized functions [1], which reduce to the singular Blakelet solution [2] as $\epsilon \to 0$. We denote this regularised *Blakelet* by $\boldsymbol{G}^B$ and employ the representation in Smith [29], which modified the typographical sign error in Ainley et al. [1].

For a flat surface with no tangential stress, such as an air-water surface with high surface tension [19], another regularized Stokeslet can be constructed as in the singular Stokeslet case,

$$ {}^{\epsilon}G^I_{ij}(\boldsymbol{x},\boldsymbol{x}_0) = {}^{\epsilon}G^S_{ij}(\boldsymbol{x},\boldsymbol{x}^0) + (\delta_{ik}-2\delta_{i3}\delta_{k3}){}^{\epsilon}G^S_{kj}(\boldsymbol{x},\boldsymbol{x}^{0*}), \tag{3.2}$$

where $\boldsymbol{x}_0^*$ is the mirror image of $\boldsymbol{x}$ with respect to the boundary, given by $\boldsymbol{x}_0^* = \boldsymbol{x}_0 - 2(\boldsymbol{x}\cdot\boldsymbol{e}_z)\boldsymbol{e}_z$ with $\boldsymbol{e}_z$ the unit vector in the z-direction. Throughout this paper, we refer to this solution (3.2) as a regularized *Imagelet*, and utilise it when considering a virtual sperm near a flat surface at $z=0$ for a fixed tangential stress associated with a shear flow, so that the perturbation of the flow field due to the swimmer does not change the tangential stress at $z=0$.

While the boundary conditions associated with fixed tangential stress and a flat surface, that is zero normal velocity, at $z=0$ may not be relevant in most physical situations, and thus similarly for the Imagelet solutions, these solutions are nonetheless very informative in assessing the extent to which hydrodynamic interactions between the surface and the cell influence the rheotactic response. Analogous comments also hold for the Stokeslet solutions.

3.1.1 The boundary integral equation of the regularised Stokeslet method

Let $p^\infty(\boldsymbol{x})$, $\boldsymbol{u}^\infty(\boldsymbol{x})$ denote the pressure and velocity field of the background shear flow, which satisfy Stokes' equations and let p, $\boldsymbol{u}$ denote the flow field for the virtual sperm in this background flow. The linearity of Stokes equations ensures that $p-p^\infty$, $\boldsymbol{u}-\boldsymbol{u}^\infty$ also satisfy Stokes equations and thus the flow velocity field around a flagellum is asymptotically approximated by the regularised Stokeslet method [14] via the boundary integral equation

$$ u_i(\boldsymbol{x}_0) - u_i^\infty(\boldsymbol{x}_0) = -\frac{1}{8\pi\mu}\int_0^L \left[{}^{\epsilon}G^{(B,I,S)}_{ji}(\boldsymbol{X}(s,t),\boldsymbol{x}_0)f_j(\boldsymbol{X}(s,t))\right] \mathrm{d}s. \tag{3.3}$$

In the above, there is summation over repeated indices, μ is the fluid viscosity, $\boldsymbol{X}(s,t)$ is the laboratory frame location of the point an arclength s along the flagellum from its proximal end-point at $\boldsymbol{\xi}(s,t)=\boldsymbol{0}$ in the flagellar reference frame, at time t, and $\boldsymbol{f}(\boldsymbol{X}(s,t))$ is an unknown stress field defined on the flagellar centreline. The integral kernel ${}^{\epsilon}G^{(B,I,S)}_{ij}$ is the regularized version of the singular Blakelet, Imagelet or Stokeslet, according to the boundary conditions imposed at $z=0$. Note that with the regularised Blakelet, the no-slip boundary conditions at $x_3=0$ is automatically satisfied by $\boldsymbol{u}-\boldsymbol{u}^\infty$

and hence $\boldsymbol{u}$ up to $O(\epsilon)$, and analogously for the tangential stress and zero normal velocity boundary conditions associated with the Imagelet. The regularization parameter, ϵ, is chosen as $\epsilon = 0.32\Delta s$ with $\Delta s = L/N$ the discretisation length of the flagellum, where the number of discretisation points along the flagellum, N, is set to be $N = 60$. These particular choices are validated when the flagellum radius varies as a curved ellipsoid with minor axis equal to $0.01L$, as detailed in Gillies et al. [14].

The flagellar location in the laboratory frame, $\boldsymbol{X}(s,t)$ is related to its location with respect to the flagellar frame, $\boldsymbol{\xi}(s,t)$, by a translation and rotation: $\boldsymbol{X}(s,t) = \boldsymbol{X}(0,t) + \boldsymbol{R}\cdot\boldsymbol{\xi}(s,t)$. Hence, the no-slip condition at location $\hat{\boldsymbol{x}}_0$ on the boundary of the flagellum, approximated by enforcing it at the nearest point on the flagellar centreline $\boldsymbol{x}_0 \equiv \boldsymbol{X}(s_0,t)$, is given by the constraint that

$$\boldsymbol{u}(\boldsymbol{x}_0) = \boldsymbol{U} + \boldsymbol{\Omega}\wedge\boldsymbol{X}(s_0,t) + \boldsymbol{R}\cdot\dot{\boldsymbol{\xi}}(s_0,t),$$

where $\boldsymbol{U}$ and $\boldsymbol{\Omega}$ are respectively the linear and rotation velocity, given by $\dot{\boldsymbol{X}}(0,t) = \boldsymbol{U}$, and $\dot{\boldsymbol{R}} = \boldsymbol{\Omega}\wedge\boldsymbol{R}$.

Thus, $\boldsymbol{u}^\infty(\boldsymbol{x}_0)$ is the known background velocity flow field and one can write $\boldsymbol{u}(\boldsymbol{x}_0)$ in terms of the flagellar waveform, specified by the known function $\boldsymbol{\xi}(s,t)$, together with a linear combination of the components of the *a priori* unknowns, $\boldsymbol{U}$, and $\boldsymbol{\Omega}$. For a collocation of the flagellar centreline with N points we thus have $3N+6$ scalar unknowns: $\boldsymbol{U}$, $\boldsymbol{\Omega}$ and the stress field $\boldsymbol{f}$ at each collocation point. Enforcing equation (3.3) at each collocation point gives $3N$ scalar equations, whilst the final 6 scalar equations required for closure are given by the fact swimming occurs with no net force and torque, a further consequence of the negligible influence of inertia for cellular microswimmers.

Neutral buoyancy is implicitly assumed in these force and torque balances, as justified by the observations of Winet et al. [36] that boundary accumulation and rheotaxis completely dominate gravitational effects, and that sperm sedimentation speeds are 1-2 orders of magnitude slower than swimming speeds. Thus gravity is safely neglected. Taking into account the repulsive potential, the required six scalar force and torque balance equations for the sperm are explicitly given by

$$0 = \int_0^L [\boldsymbol{f} + \boldsymbol{f}^{rep}]\,\mathrm{d}s = \int_0^L \boldsymbol{X}\wedge[\boldsymbol{f} + \boldsymbol{f}^{rep}]\,\mathrm{d}s, \tag{3.4}$$

where $\boldsymbol{f}^{rep}$ is the force density due to the repulsive potential.

We refrain from using DVLO theory to determine this potential as this has been observed to be inaccurate with increasing osmolarity, even before physiological isotonicity is achieved [26], since the Debye layer shrinks to nanometer scales and other interactions dominate the surface interactions between the cell and a solid surface on the scale of tens to one hundred nanometres. Hence instead a simple repulsive potential, as also used by Spagnolie et al. [32], is implemented with

$$\boldsymbol{f}^{rep}(\boldsymbol{x}) = g\frac{e^{-z/d}}{1-e^{-z/d}}\boldsymbol{e}_z, \tag{3.5}$$

arising from non-hydrodynamical interactions, such as van der Waals forces, at $z = 0$. The parameters are presented in *Supplementary Information*, Table 1, and with this choice of $d = 0.005L$, sperm swimming is prohibited within a distance of approximately $0.01L = 2d$ from $z = 0$. As can be seen in Fig. 2(d)(e) changes in d do affect the surface induced-trajectory curvature as the cell boundary accumulation height changes, though we cannot distinguish a choice of d given the available data and, in any case, the surface repulsion potential is highly variable [22]. Nonetheless the qualitative conclusions are unaffected and thus so are the conclusions drawn in the main text.

Finally, the $3N+6$ scalar algebraic equations associated with a collocation point discretisation of (3.3) and (3.4) at a fixed point in time are subjected to singular preconditioning prior to solution via an LU factorisation. This yields the unknown surface stress $\boldsymbol{f}$ and, more importantly for our purposes, the linear and the angular velocities, $\boldsymbol{U}$ and $\boldsymbol{\Omega}$ at a fixed point in time. Thus the sperm position and orientation can be updated using these velocities. Iterating this process, which is performed via Heun's method [30, 20, 21], the sperm trajectory is generated, allowing the exploration of sperm boundary accumulation and rheotaxis.

3.2 Scheme validation

3.2.1 A comparison with other algorithms

For the validation of the RSM scheme above, we evaluated the swimming velocity during one beat cycle of a headless sperm flagellum in the absence of a surface repulsion potential or a boundary at $z = 0$. In addition we use the parameters

$$\alpha = 0,\ B = 1/2\pi,\ k = 2\pi,\ \omega = 1/2\pi,$$

with length and time in units of the flagellar length L and beat period T whilst the cell is initially located so that the body-fixed and the laboratory frame coincide. In Figure 1 these results for the RSM algorithm are compared with those obtained from Johnson's slender-body theory (SBT), as documented in Smith et al. [30], and direct numerical computation via the boundary element method (BEM), as detailed in Ishimoto & Gaffney [20, 21], analogously to the validation studies within Gillies et al. [14]. Figure 1 indicates the RSM scheme provides sufficient accuracy to analyse and discuss cell movement. More generally, mechanically based models have been shown to produce agreement with observation using flagellar waves extracted from video-microscopy, for instance [12, 14], emphasising that understanding sperm swimming can often be reasonably considered in terms of mechanics.

We also briefly note that it is inappropriate to quantitatively compare the regularised Stokeslet results here to the multi-particle collision results presented by Elgeti et al. [9, 10] and the slender body theory results of Smith et al., [30, 31] for the purposes of validation as the representation of surface forces differs across all three papers. In addition this entails that the results presented in this manuscript should not be used to distinguish between the discrepancy in the conclusions of Elgeti et al. [9] and Smith et al., [30], as documented in a correspondence [10, 31], whereby Elgeti et al. conclude that hydrodynamic flow fields induce sperm surface capture at much closer distances than Smith et al., who report boundary accumulation heights of very roughly 10 microns for a planar beater. Furthermore, we also note the results in the main text predict both larger mean boundary accumulation heights (main text, Fig 5b, red and orange curves, with mean boundary accumulation heights of about 8.5 microns) and also much closer surface swimming (Fig 5b, blue curve). Hence, even neglecting the absence of control for the surface forces, the results once more cannot be used to distinguish the discrepancy reported in the correspondence between Elgeti et al. and Smith et al. [9, 31].

3.2.2 A comparison with observations

We proceed to consider the behaviour of a virtual mouse sperm with no head and an elliptical helicoidal waveform near a no-slip surface at $x_3 \equiv z = 0$, in the absence of a background shear flow, with the

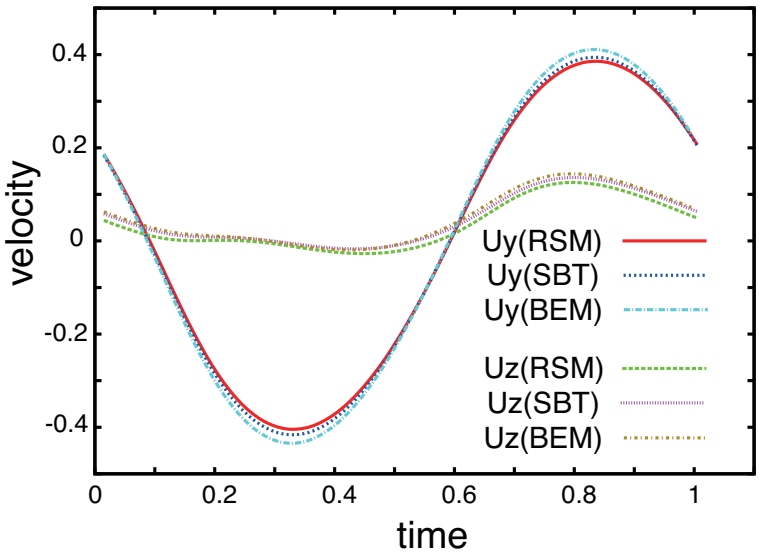

Figure 1: The linear velocity of the model spermatozoon during one beat cycle with three different numerical schemes: the regularized Stokeslet method (RSM), Johnson's slender-body theory (SBT), and direct numerical simulation via the boundary element method (BEM). Figure axes are non-dimensionalised using the flagellum length L as the lengthscale and the beat period T as the timescale.

parameters of Table 1, except that the flagellar length is $L = 120\mu$m, matching that of CD1 mice [34]. We further use a chirality parameter of $\alpha = 0.2$, matching the parity of mouse sperm chirality, and take $\Gamma = \infty$ so that the flagellar waveform is symmetric; the waveform is fully specified by equation (2.1) of the main text. A surface repulsion force, as given by equation (3.5) is also present in these simulations.

As generally the case with flagellar waveforms with non-trivial chirality, this virtual sperm is predicted to roll as it swims rather than asymptoting to a fixed orientation relative to the laboratory frame. Furthermore, boundary accumulation is predicted with the virtual sperm swimming adjacent to the no slip surface such that the axis of symmetry associated with the elliptical helicoidal waveform is rotated; hence the flagellar envelope is just offset from parallel to the no slip surface, as shown in Fig 2b. This gives a good qualitative comparison to Fig 2a, which is the sideview of flagellar beat patterns presented by Woolley as an illustration of the typical conical helicoid flagellar beat pattern exhibited by sperm near a no-slip surface [38]. Note however that these observations were made from above the cover slip but presented in a sideview, and thus assumed sufficient symmetry of the waveform, as is the case for a perfect conical helicoid. However, clearly Woolley's images suffer from making this approximation in that the flagellum penetrates the surface. In addition this alignment with a no-slip boundary for a sperm with an elliptical helicoid beat pattern is also seen in the slender body simulations of Smith et al. [30], though these latter simulations cannot be continued once the sperm approaches the surface, due to sperm crashing as no repulsion surface potential force is considered.

Woolley [38] also presented the projection of the trajectories of CD1 mouse sperm onto the no-slip surface, as reproduced in Fig 2c, with the analogous predictions for the virtual sperm presented in Fig 2d. Note that the direction of the predicted circling in Fig 2d agrees with observation, as does the presence of a lateral oscillatory displacement about the mean trajectory. Furthermore, the idealised

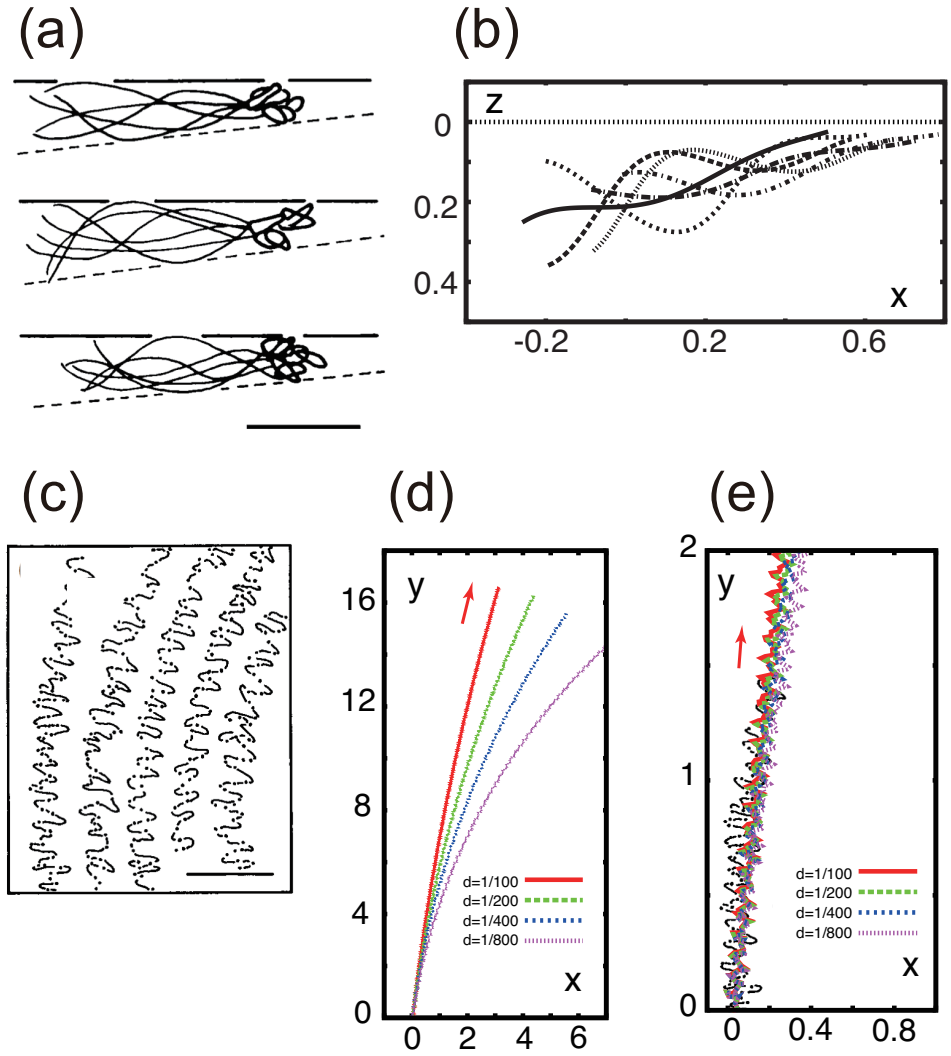

Figure 2: Sperm dynamics with elliptical helicoid beating, but no shear flow. (a) Observations of an elliptical helicoid beat at snapshots in time for individual Chinchilla sperm, scale bar 25μm [38]. (b) Snapshots of the elliptical helicoid beat, in sideview, for a virtual mouse sperm, which is predicted to swim adjacent to a no-slip boundary at $z = 0$; the simulations use the parameters given in Table 1 except that $L = 120\mu$m, the length of CD1 mice sperm observed by Vernon and Woolley [34]. In addition, the parameter choice of a symmetric flagellar wave with positive chirality was used, with $\Gamma = \infty$, $\alpha = 0.2$, $\boldsymbol{X}(s = 0, t = 0) = (0, 0, 0.1)$ and the initial inclination of the flagellum relative to the no slip plane at $z = 0$ was taken to be $\theta_{init} = 0.2\pi$. The snapshots for times t, given by $t/T \in \{10, 11, \ldots 15\}$, are superimposed, where T is the beat period. (c) The observed trajectories of CD1 mouse sperm, viewed from above, after accumulating at an upper coverslip [38]; scale bar 50μm. (d) The corresponding trajectory from computational simulations for the virtual CD1 mouse sperm used to generate plot (b), after projection onto the plane of the no-slip surface with an arrow depicting the direction of sperm swimming and the effect of varying d, in units of the flagellar length, L, depicted. (e) The trajectory of the lefthand trajectory of observed CD1 mice sperm in plot (c) is traced on the computed trajectory of virtual CD1 mice sperm for these different vales of d. Finally note that unit of length in plots (b), (d) is given by CD1 mouse flagellar length $L = 120\mu$m, and that (a), (c) have been reproduced from Woolley [38], with permission (Licence No. 3596460518634, Copyright © 2003, Society for Reproduction and Fertility).

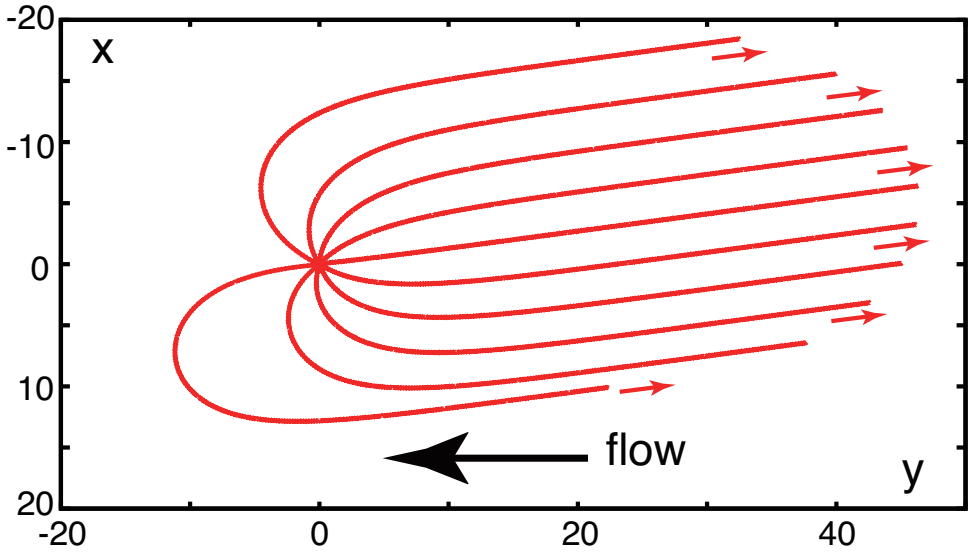

Figure 3: The effect of initial orientation on sperm trajectories for elliptical helicoid beating in a background flow, whose direction is depicted by the large arrow. The virtual sperm swimming trajectories are projected onto the x-y plane, with all axes in units of flagellum length, L. The simulations use the parameters presented in Table 1, with $\Gamma = \infty$ and $\alpha = 0.2$, and the cells are initially located at $\boldsymbol{X}(s = 0, t = 0) = (0, 0, 0.1L)$ with a trivial initial attack angle, $\theta_{init} = 0$, and thus are oriented parallel to the x-y plane. The initial orientation of the virtual sperm within the x-y plane however is taken from the values $\{0, 0.2\pi, \ldots, 1.8\pi\}$ and the resulting projections of the cell trajectories are plotted on the x-y plane, with small arrows depicting the direction of swimming.

waveform produces a trajectory that essentially agrees with observation, as shown in Fig 2e, where the leftmost trajectory of Fig 2c is superimposed with the trajectories of Fig 2d, after rescaling so that the lengthscales of each figure match. The only discrepancy is that the extent of the lateral displacement in the trajectory is slightly underestimated by the virtual sperm simulations, most likely due to our use of an idealised waveform; in particular note that prior studies demonstrating quantitative agreement featured the extraction of flagellar waveforms from video-microscopy. Nonetheless, here we observe predictions for the swimming sperm trajectory that qualitatively match observed trajectories for a number of CD1 mice sperm, overlapping with one from the cell sample in terms of the “value-averaged path” used in sperm diagnostics [35], which neglects lateral displacement as this does not contribute to sperm propagation on longer timescales.

4 The trajectories of sperm with different initial orientations

In the main text, the virtual sperm is initially oriented so that the ξ_3 axis coincides with x axis; this constraint is nonetheless without loss of generality. In Fig. 3, simulations for sperm with a symmetrical helical beat ($\Gamma = \infty, \alpha = 0.2$) and different initial orientations are shown. The virtual cells are always initially located at $\boldsymbol{X}(s = 0, t = 0) = (0, 0, 0.1L)$ with a no-slip boundary at $z = 0$, a background shear flow and trivial initial attack angle, $\theta_{init} = 0$, so that the cells are initially parallel to the x-y

plane. All further parameters are as in Table 1, though the initial direction of the sperm within the x-y plane is varied such that the angle made by the flow direction and initial sperm orientation takes the values $\{0, 0.2\pi, \ldots, 1.8\pi\}$. This includes an initial orientation directly into, and directly away from, the background flow. The resulting trajectories, as presented in Fig. 3, emphasise that the initial direction of the sperm does not affect the basic dynamics of sperm rheotaxis, as all trajectories ultimately exhibit the same asymptotic direction for the projection onto the x-y plane.

5 The trajectories of sperm with an asymmetric beat pattern and small chirality

Consider an asymmetric beat as illustrated in Fig. 1b of the main text. As observed in various marine species spermatozoa, such as sea urchin and *Ciona* [23, 27], an extensively asymmetric planar flagellar beat leads to a circling trajectory, in which the direction of the orbit is often selected so that all the cells rotate in the same direction. This selection is considered to be driven by a small chirality of the flagellar beat [18]. We explore the swimming trajectory of the asymmetric beating flagella in Fig. 4 using the parameters of Table 1, with $\Gamma = 0.5$, and a range of chiralities, $\alpha \in \{0, \pm 0.001, \pm 0.01\}$. The cell is initially located at $(0, 0, L)$ with the initial angle $\theta_{init} = 0$, so that it is oriented parallel to the laboratory x-y plane $z = 0$, which is a no-slip boundary in the simulations, and the surface repulsive potential force, equation (3.5), is also imposed.

The trajectory of the sperm with a planar beat ($\alpha = 0$, red curve) is a closed planar circle with transverse oscillations and a counterclockwise swimming direction when viewed above. With a slight chirality, the projected trajectory is not appreciably altered, though there is a slow drift in the z direction, which is reversed with a change in the sign of the chirality. With a further increase of the magnitude of chirality, the perpendicular drift is increased. Thus the counter-clockwise circling trajectory near a bottom boundary can only be found in a cell with a positive chirality, as negative chirality cells would not approach this boundary. If there was a no-slip boundary, for instance a coverslip, at $z =$ constant > 1, the negative chirality cell would approach the coverslip and thus exhibit a counter-clockwise rotation when viewed from above, corresponding to a clockwise trajectory viewed from the fluid, namely the opposite rotation direction to cells with positive chirality. Hence chirality is predicted to select the observed rotational direction for such swimmers. As a final remark, with a further increase in the magnitude of the chirality, the sperm trajectory becomes straighter, and thus tight circling in one direction near a boundary is only observed when the flagellar beat is both strongly asymmetric and nearly planar.

6 Estimates of rheotactic criteria

Sea Urchin Sperm Consider the sperm of the sea urchin Lytechinus, which have with $L \approx 45\mu$m, [4], a planar beat of frequency $\omega \approx 30$Hz and a swimming speed of 160μm [3]. Assuming a shear free turning circle of radius $R_{turn} \approx 25\mu$m, which is intermediate in the range reported by Woolley and Vernon [37] and Miki and Clapham [23], the above rheotactic condition for planar beaters, $\mathcal{R} := UR_{turn}/[L\omega H] \gg 4$ requires that the accumulation height satisfies $H \ll 750$nm. Furthermore the shear rate must be increased to beyond $\mathcal{S} := \dot{\gamma} R_{turn}/[\omega L] \gg 4$, and thus there is a lower bound of

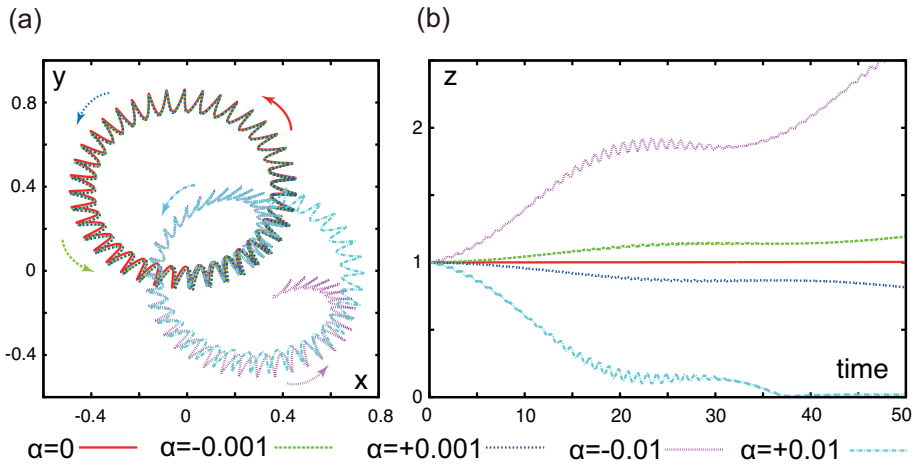

Figure 4: Sperm dynamics with an asymmetric beat pattern, but no shear flow. The simulations use the parameters given by Table 1, with $\Gamma = 0.5$ and α as depicted. The cells are initially located at $\boldsymbol{X}(s = 0, t = 0) = (0, 0, L)$ with the initial angle $\theta_{init} = 0$, and thus oriented parallel to the x-y plane. The no-slip boundary condition is imposed on $z = 0$, together with the repulsive surface potential force and all axes are in units of flagellum length, L, in the plots. (a) The projection of the sperm trajectories onto the x-y plane, which corresponds to trajectories viewed from above. All the cells reveal counter-clockwise rotation, reflecting the asymmetric beat. (b) Time evolution of z, the vertical distance above the no-slip boundary, for these cells.

the shear rate required for rheotaxis, $\dot{\gamma} \gg 140\text{s}^{-1}$. Firstly the accumulation height is much less than the lengthscale of the sea urchin sperm head, as deduced by inspection of the micrographs in [3]. Secondly, observed shear rates between murine ampulla mucosal folds are substantially less than 1s^{-1} by inspection of Fig 1d in [23] and thus these values of $\dot{\gamma}$ are orders of magnitude beyond the female reproductive tract flows that that have guided experimental scales. Consequently the absence of sea urchin rheotaxis in observational studies [23] is consistent with the modelling predictions.

CatSper-KO Sperm The CatSper-KO mouse spermatozoa examined in Miki & Clapham [23] were CatSper1 null and did not rheotax whilst presenting with circular rotation near a substrate. We assume mouse sperm parameters, $L \approx 80\mu$m [7], with a CatSper1 null mutant angular beat frequency of $\omega = 2\pi/T \approx 30$Hz, where T is the beat period, as reported by Carlson et. al. [5] in terms of the frequency $f = 1/T$ which was in the range [4Hz-8Hz]. From the observation of supplemental information videos presented by Miki and Clapham [23] we also have $U \approx 36\mu$m/s [23], and the shear-free turning circle radius is $R_{turn} \approx 40\mu$m. An estimation of the rheotactic criteria reveals that the accumulation height must satisfy $H \ll 150$nm and the shear rate must satisfy $\dot{\gamma} \gg 240\text{s}^{-1}$. Once more these constraints differ by orders of magnitude from the conditions in Miki and Clapham's experimental studies and thus the absence of rheotaxis is predicted, consistent with observation.

Hyperactivated Sperm Hyperactivated human sperm beat with a frequency of about $\omega \sim 15$Hz [24] whilst star-spin hyperactivated human sperm in media [25] exhibit tight circling on the scale of roughly 30 microns [33]; combined with the human flagellum length of 56μm rheotaxis requires shear rates on the scale $\dot{\gamma} \gg 30\text{s}^{-1}$ which is over a magnitude larger than the observed physiological and experimental scales. Hence rheotaxis is predicted to be absent under such conditions. In contrast, the

hyperactivation of mouse sperm in viscous solution, leads to much straighter swimming in Miki and Clapham's studies [23], indicating that rheotaxis would be predicted to occur, at least if boundary accumulation is present. However, the turning circle radius of these cells in the same study [23] is difficult to estimate given the limited length of the trajectories captured, and most likely highly variable preventing a more precise statement.

References

[1] J. Ainley, S. Durkin, R. Embid, P. Boindala, and R. Cortez. 2008, The method of images for regularised Stokeslets. *J. Comput. Phys.*, **227**, 4600–4616.

[2] J. R. Blake. 1971, A note on the image system for a stokeslet in a no slip boundary. *Proc. Camb. Phil. Soc.*, **70**, 303–310.

[3] C. J. Brokaw. 1965, Non-sinusoidal bending wave of sperm flagella. *J. Exp. Biol.* **43**, 155–169.

[4] C. J. Brokaw. 1991, Microtubule sliding in swimming sperm flagella - direct and indirect measurements on sea-urchin and tunicate spermatozoa. *J. Cell Biol.* **114**, 1201–1215.

[5] A. E. Carlson, R. E. Westenbroek, T. Quill, D. Ren, D. E. Clapham, B. Hille, D. L. Garbers, D. F. Babcock. 2003, CatSper1 required for evoked Ca^{2+} entry and control of flagellar function in sperm *Proc. Natl. Acad. Sci. U.S.A.*, **100**,14864–14868.

[6] R. Cortez. 2001, The method of regularized stokeslets. *SIAM J. Sci. Comput.* **23**, 1204–1225.

[7] J. M. Cummins and P. F. Woodall. 1985, On mammalian sperm dimensions. *J. Reprod. Fert.*, **75**,153–175.

[8] R. D. Dresdner and D. F. Katz. 1981, Relationships of mammalian sperm motility and morphology to hydrodynamic aspects of cell function. *Bio. Reprod.*, **25**, 920–930.

[9] Elgeti J, Kaupp UB, Gompper G. 2010, Hydrodynamics of sperm cells near surfaces. *Biophys. J.*, **99**, 1018–1026.

[10] Elgeti J, Kaupp UB, Gompper G. 2011, Response to comment on article: Hydrodynamics of sperm cells near surfaces. *Biophys. J.*, **100**, 2321–2324.

[11] D. W. Fawcett. 1975, The mammalian sperm. *Dev. Biol.*, **44**, 394–436.

[12] B. M. Friedrich, I. H. Riedel-Kruse, J. Howard, and F. Juelicher. 2010, High-precision tracking of sperm swimming fine structure provides strong test of resistive force theory. *J. Exp. Biol.*, **213**, 1226–1234, 2010.

[13] E. A. Gaffney, H. Gadêlha, D. J Smith, J. R. Blake, J. C Kirkman-Brown. 2011, Mammalian Sperm Motility: Observation and Theory, *Ann. Rev. Fluid Mech.*, **43**, 501-528.

[14] E. Gillies, R. M. Cannon, R. B. Green, and A. A. Pacey. 2009, Hydrodynamic propulsion of human sperm. *J. Fluid Mech.*, **625**, 445–474.

[15] J. Gray and G. J. Hancock. 1955, The propulsion of sea urchin spermatozoa. *J. Exp. Biol.*, **32**, 802–814.

[16] S. Ishijima, S. Oshio, and H. Mohri. 1986, Flagellar Movement Of Human-Spermatozoa. *Gamete Res.*, **13**, 185–197.

[17] S. Ishijima, M. S. Hamaguchi, M. Naruse, S. A. Ishijima, and Y. Hamaguchi. 1992, Rotational movement of a spermatozoon around its long axis. *J. Exp. Biol.*, **163**, 15–31.

[18] S. Ishijima, and Y. Hamaguchi. 1992, Relationship between direction of rolling and yawing of golden hamster and sea urchin spermatozoa. *Cell Struct. Funct.*, **17**, 319–323.

[19] K. Ishimoto and E. A. Gaffney. 2013 Squirmer dynamics near a boundary. *Phys. Rev. E*, **88**, 062702.

[20] K. Ishimoto and E.A. Gaffney. 2014, Swimming efficiency of spherical squirmers: Beyond the Lighthill theory. *Phys. Rev. E*, **90**, 012704.

[21] K. Ishimoto and E. A Gaffney. 2014, A study of spermatozoan swimming stability near a surface. *J. Theor. Biol.*, **360**, 187–199.

[22] J. D Klein, A. R. Clapp, and R. B. Dickinson. 2003, Direct measurement of interaction forces between a single bacterium and a flat plate. *J. Coll. Interface Sci.*, **261**, 379–385.

[23] K. Miki and D. E. Clapham. 2013, Rheotaxis Guides Mammalian Sperm. *Curr. Biol.*, **23**, 443–452.

[24] E. H. Ooi, D. .J Smith, H. Gadêlha, E. A. Gaffney, J. Kirkman-Brown. 2014, The mechanics of hyperactivation in adhered human sperm. *J. Roy. Soc. Open Science*, **1**, 140230.

[25] L. Robertson, D. P Wolf, and J. S Tash. 1988, Temporal Changes In Motility Parameters Related To Acrosomal Status - Identification And Characterization Of Populations Of Hyperactivated Human-Sperm. *Biol. Reprod.*, **39**, 797–805.

[26] Sharp JM, Dickinson RB. 2005, Direct evaluation of DLVO theory for predicting long-range forces between a yeast cell and a surface. *Langmuir*, **21**, 8198–8203.

[27] K. Shiba, S. A. Baba, T. Inoue, and M. Yoshida. 2008, Ca^{2+} bursts occur around a local minimal concentration of attractant and trigger sperm chemotactic response . *Proc. Natl. Acad. Sci. U.S.A.*, **105**, 19312–19317.

[28] D. J. Smith, E. A. Gaffney, H. Gadhêla, N. Kapur, and J. C. Kirkman-Brown. 2009, Bend propagation in the flagella of migrating human sperm, and its modulation by viscosity. *Cell Motil. Cytoskel.*, **66**, 220–236.

[29] D. J. Smith. 2009, A boundary element regularized Stokeslet method applied to cilia- and flagella-driven flow *Proc. Roy. Soc. A*, **465**, 3605–3626.

[30] D. J. Smith, E. A. Gaffney, J. R. Blake, and J. C. Kirkman-Brown. 2009, Human sperm accumulation near surfaces: a simulation study. *J. Fluid Mech.*, **621**, 289–320.

[31] Smith DJ, Gaffney EA, Shum H, Gadêelha H, Kirkman-Brown J. 2011, Comment on the article by J. Elgeti, U. B. Kaupp, and G. Gompper: Hydrodynamics of sperm cells near surfaces. *Biophys. J.*, **100**, 2318–2320.

[32] S. E Spagnolie and E. Lauga. 2012, Hydrodynamics of self-propulsion near a boundary: predictions and accuracy of far-field approximations. *J. Fluid Mech.*, **700**, 105–147.

[33] T. Su, L. Xue and A. Ozcan. 2012, High-throughput lensfree 3D tracking of human sperms reveals rare statistics of helical trajectories. *Proc. Natl. Acad. Sci. U.S.A.*, **109**, 16018–16022.

[34] G. G. Vernon and D. M. Woolley. 2002 Functional state of the axonemal dyneins during flagellar bend propagation. *Biophys. J.*, **83**, 2162–2169.

[35] WHO. 2010 *World Health Organization, Department of Reproductive Health and Research. WHO laboratory manual for the Examination and processing of human semen.* World Health Organization.

[36] H. Winet, G. S. Bernstein, and J. Head. 1984, Observations on the response of human spermatozoa to gravity, boundaries and fluid shear. *J. Reprod. Fert.*, **70**, 511–523.

[37] D. M. Woolley, G. G. Vernon. 2001, A study of helical and planar waves on sea urchin sperm flagella, with a theory of how they are generated. *J. Exp. Biol.* **204**, 1333–1345.

[38] D. M. Woolley. 2003, Motility of spermatozoa at surfaces. *Reproduction*, **126**, 259–270.